Research Square

Preprints are preliminary reports that have not undergone peer review.
They should not be considered conclusive, used to inform clinical practice,
or referenced by the media as validated information.

ETS2/c-Jun Inflammatory Storm Interceptor: Smart Dual-Responsive Temporal Regenerative Engine Reprograms Degenerative Nucleus Pulposus Microenvironment

Yusen Qiao

qiaoyusen8612@suda.edu.cn

The First Affiliated Hospital of Soochow University https://orcid.org/0000-0003-2441-6687

Jinhao Ni

The Second Affiliated Hospital of Soochow University

Haifu Sun

Shanghai Tenth People's Hospital of Tongji University

Kang Wei

Tongji Hospital of Huazhong University of Science and Technology

Xiaowei Zhang

The Second Affiliated Hospital of Soochow University

Yuexing Wang

The Second Affiliated Hospital of Soochow University

Yu Chen

The First Affiliated Hospital of Soochow University

Haowen Lu

The First Affiliated Hospital of Soochow University

Minbo Jian

The First Affiliated Hospital of Soochow University

Zijie Zhou

The Second Affiliated Hospital of Soochow University

Lei Sheng

The Second Affiliated Hospital of Soochow University

Xiaozhong Zhou

Second Affiliated Hospital of Soochow University Department of Orthopaedic Surgery

Bin Li

Suzhou Medical College, Soochow University https://orcid.org/0000-0001-8516-9953

Jun Dai

The Second Affiliated Hospital of Soochow University

Article

Keywords: ETS2, c-Jun, temporal regeneration, dual response, microsphere, injectable hydrogel, nucleus pulposus, intervertebral disc degeneration

Posted Date: July 13th, 2026

DOI: https://doi.org/10.21203/rs.3.rs-10212413/v1

License: This work is licensed under a Creative Commons Attribution 4.0 International License.
Read Full License

Additional Declarations: There is **NO** Competing Interest.

ETS2/c-Jun Inflammatory Storm Interceptor: Smart Dual-Responsive Temporal Regenerative Engine Reprograms Degenerative Nucleus Pulposus Microenvironment

Jinhao Ni[1,2#], Haifu Sun[4#], Kang Wei[5#], Xiaowei Zhang[1], Yuexing Wang[1], Yu Chen[3], Haowen Lu[3], Minbo Jian[3], Zijie Zhou[1], Lei Sheng[1], Xiaozhong Zhou[1], Bin Li[6*], Yusen Qiao[3*], Jun Dai[1*]

[1]Department of Orthopedic Surgery, The Second Affiliated Hospital of Soochow University, Suzhou, Jiangsu 215004, China.

[2]School of Physical Education, Sichuan University, Chengdu, Sichuan 610041, China.

[3]Department of Orthopedics, The First Affiliated Hospital of Soochow University, 188 shizi Street, Suzhou, Jiangsu 215006, China.

[4]Department of Orthopedics, Shanghai Tenth People's Hospital, School of Medicine, Tongji University, Shanghai 200072, China.

[5]Department of Dermatology, Tongji Hospital, Tongji Medical College, Huazhong University of Science and Technology, 1095 Jiefang Ave, Wuhan, Hubei 430030, China.

[6]Medical 3D Printing Center, Orthopedic Institute, Department of Orthopedic Surgery, The First Affiliated Hospital, School of Basic Medical Sciences, Interdisciplinary Innovation Center for Nanomedicine, MOE Key Laboratory of Geriatric Diseases and Immunology, Suzhou Medical College, Soochow University, Suzhou, Jiangsu 215000, PR China.

[#] J. Ni, H. Sun and K. Wei contributed equally to this work.

Abstract

Intervertebral disc degeneration (IDD) is a major cause of low back pain, yet effective disease-modifying therapies remain elusive. Here we identify ETS2 as a key driver of IDD, demonstrating its upregulation in human degenerated discs and establishing that the ETS2/c-Jun axis promotes IDD both *in vitro* and *in vivo*. Although ETS2 inhibitor—MEK inhibitor (MEKi) attenuates IDD, narrow therapeutic window and systemic toxicity limit its translational potential. To address this, we engineer a pH- and reactive oxygen species (ROS)-dual-responsive hydrogel microsphere incorporating a "temporal regenerative engine" that enables microenvironment reprogramming and

functional restoration. This system conjugates citric acid and MEKi-encapsulated liposomes, featuring a biphasic release mechanism: a rapid ROS-responsive module delivers MEKi to quench the inflammatory storm, followed by a sustained pH-responsive module releasing citric acid to provide metabolic support and antioxidant defense, mirroring the physiological "anti-inflammation first, then reconstruction" repair sequence. Following *in situ* injection in SD Rat coccygeal vertebra acupuncture model, the microspheres achieve sustained drug delivery with reduced cytotoxicity, suppress the ETS2/c-Jun axis, resolve inflammation, clear ROS, delay cellular senescence, and restore aggrecan and type II collagen synthesis, ultimately enabling functional disc regeneration. This "temporal control-microenvironment reprogramming-functional regeneration" paradigm offers a promising strategy for IDD regenerative medicine.

Keywords: ETS2; c-Jun; temporal regeneration; dual response; microsphere; injectable hydrogel; nucleus pulposus; intervertebral disc degeneration

Introduction

Intervertebral disc degeneration (IDD), an age-associated degenerative disorder, represents a significant global health challenge [1]. Epidemiological studies indicate that 632 million people suffer from low back pain(LBP) [2], and 85% of people in the northern hemisphere are expected to experience the disease in their lifetime [3]. The current clinical treatments for IDD including conservative treatments and surgical interventions focus on alleviating pain and symptoms rather than arresting progression of IDD or restoring disc function [4]. This leads to a need for biological reprogram that can restore the structural integrity and biomechanics of degenerated intervertebral discs (IVDs). The disease burden extends beyond individual morbidity, with IDD and its associated pathologies imposing substantial strain on healthcare infrastructure and socioeconomic systems.

The main features of IDD are decrease in the height of the intervertebral discs and hydration, and reduced ability to absorb stress loads [5], in which inflammatory cytokines and reactive oxygen species (ROS) play a significant mediating role [6,7]. Nucleus

pulposus (NP) is the central tissue originating from the embryonic notochord and is rich in a hydrophilic proteoglycan molecule that gives hydration to the intervertebral disc [8]. As degeneration progresses, inflammatory cytokine levels increase, aggrecan and collagenII degradation are enhanced, and then nucleus pulposus cells (NPCs) phenotypes change [6].

ETS2 (a member of the E26 transformation-specific sequence [ETS] domain family) [9] is a central regulator of human inflammatory macrophages, and its regulated genes are prominently expressed in diseases such as inflammatory bowel disease, ankylosing spondylitis, primary sclerosing cholangitis, and gaugandre arteritis [10]. ETS2 signaling plays a central role in a variety of inflammatory diseases [10]. The upstream of ETS2 is regulated by ERK1/2 [9], and overexpression of ETS2 in resting macrophages can upregulate multiple drug targets, including TNF and IL-23 [10]. PD-0325901, a selective non-ATP-competitive MEK inhibitor (MEKi), shows potent anti-inflammatory activity against inflammatory macrophages, disrupting ETS2 effects [10]. Meanwhile, PD0325901 can enhance the effect of kaempferol in inhibiting ERK1/2 phosphorylation, downregulating expression of MMP3 and ADAMTS4, and upregulating expression of aggrecan and collagen II, assisting in alleviating the process of IDD [11].

C-Jun is an important member of the activating protein-1 (AP-1) transcription factor family, encoded by c-Jun gene, with a conserved basic DNA binding domain and the bZIP region [12], which regulates gene expression by forming homodimers or by forming heterodimers with proteins such as c-Fos [13,14]. C-Jun tends to bind to inflammation-related genes. In macrophages, c-Jun binds to the Cxcr3 promoter region to regulate inflammatory and metabolic programs [15]. In IDD, c-Jun is activated by JNK, inducing the release of pro-inflammatory cytokines, resulting in apoptosis of NPCs and degradation of ECM [16,17]. It is reported that ETS2 can specifically bind to c-Jun, but the downstream mechanism have not been expounded [18].

Gelatin methacryloyl (GelMA) is a gelatin derivative, and its precursor, the natural substance gelatin, is primarily a denatured collagen product [19,20] with better solubility and lower antigenicity [21]. GelMA hydrogels have been widely applied in tissue engineering due to their excellent biocompatibility, tunable mechanical properties,

light-curing properties, and biological activity [22]. Despite these important characteristics exhibited by hydrogels, there are still many drawbacks, such as low mechanical strength, low thermal stability, and fast degradation rates, which limit their effective utilization [22,23]. Recent advancements in GelMA have mainly focused on combining it with bioactive nanomaterials and functional nanomaterials to enhance the physical, chemical, and biological properties of GelMA [22].

In the process of IDD, microenvironmental changes such as pH changes [24] and ROS accumulation [25] are the main characteristics. The hypoxic microenvironment induces anaerobic metabolism in NPCs, and persistent hypoxia and glycolysis lead to lactate accumulation, resulting in a decrease in pH in IVD [24]. 3-Acrylamidophenylboronic acid (APBA) belongs to boric acid monomer compound [26]. DSPE-TK-PEG is a composite nanomaterial composed of distearoylphosphatidylethanolamine (DSPE), ketogenic thiol (TK) fragments and polyethylene glycol (PEG). It combines membrane fusion of phospholipids, ROS response of TK, and hydrophilicity and biocompatibility of PEG to form a material with physicochemical properties and a wide range of potential application value. PEG can form borate bonds with phenylboronic acid bonds of APBA, which imparts pH responsiveness to the hydrogel, senses pH changes and releases drugs.

The senescence of NPCs is associated with dysfunction of mitochondria, which play a key role in homeostasis in various cell types [27,28]. IDD, mechanical damage, cytokine induction, and other stimuli can cause damage to mitochondria in NPCs, inducing the production of ROS, which in turn leads to increased cellular inflammation, metabolic disturbances, and enhanced apoptosis [29,30]. During primary ROS response, TK units in nanomedicine can be effectively cleaved by overexpressed ROS at degenerative intervertebral disc, which not only depletes ROS at the lesion site, but also triggers the controlled release of MEKi specificity in inflammatory tissues to exert anti-inflammatory effects [31]. Citric acid (CA) can enhance the mechanical properties and biological activity of hydrogels as a natural antioxidant and crosslinker [32]. NPCs are located in a closed, nonvascular, hypoxic acidic environment, and their primary mode of energy supply is glycolysis [33]. The citric acid cycle is involved in the process of IDD, correcting the metabolic pathways related to the metabolism of the citric acid cycle, increasing ATP production, inhibiting the IDD process, and normalizing the

metabolomics pathway [34,35].

Herein, in this study, we propose an injectable hydrogel (GAC@LTM) with a dual-response system based on pH and ROS and sustainable drug release, which was composed of GelMA encapsulating APBA and CA, with DSPE-TK-PEG connected to APBA via Borate bonds. The other end of DSPE-TK-PEG is embedded with liposomes, where MEKi is encapsulated. This GAC@LTM hydrogel microsphere is expected to exert anti-inflammatory and anti- senescence effect in the process of IDD from the perspectives of both pH response of Borate bonds between APBA and DSPE-TK-PEG, and ROS response of TK and CA. We discovered that GAC@LTM reduced matrix remodeling and oxidative stress level both in vitro and in vivo, improving NPC microenvironment and alleviated NPC degeneration. Simultaneously, the process of GAC@LTM reprogram was also accompanied by inhibition of inflammatory response and catabolism, and significantly improved anabolism. Mechanically, this GAC@LTM was able to enhance NP regeneration via suppress the TNF/ETS2/c-Jun cascade axis, with ETS2 as key transcription factor, resisting inflammation and oxidative stress. Finally, we established IDD rat model and confirmed that GAC@LTM could recover disc height, inhibit inflammation and oxidative stress and promote regeneration of degenerated intervertebral discs. We believe this dual-responsive injectable hydrogel will pave a new way for alleviating inflammation and NP regeneration in the process of IDD.

We are committed to building dual-response hydrogel systems with "Temporal Regenerative Engine" properties, whose sophisticated timing control mechanisms perfectly mimic and guide the dynamic process of tissue physiological repair. The dual response design of the system realizes the spatiotemporal precision of the reprogram strategy. In the acute phase, ROS rapid response module (thioether bond breakage) immediately removes reactive oxygen radicals such as hydrogen peroxide, and simultaneously explosively releases MEK inhibitors to block inflammatory storms and effectively curb microenvironment deterioration. During the chronic repair phase, the pH-sensitive module (carboxyl protonation) continuously releases metabolic support factors such as CA, enhances cellular energy metabolism by providing tricarboxylic acid cycle intermediates, and synergistically maintains long-term antioxidant defense.

For the first time, it reproduces the natural sequential logic in the physiological repair process at the molecular level, breaks through the limitation of "transient release" of traditional drug delivery system, successfully reprograms the degenerative microenvironment from a self-sustaining vicious cycle to a self-reinforcing regenerative cycle, and sets a new standard for the development of the next generation of "space-time regulation" regenerative medicine products.

Results

ETS2 is highly expressed in degenerated NP tissue

We conducted RNA transcriptome sequencing analysis on normal NPCs and inflammatory NPCs. The results showed that the expression level of ETS2 in the inflammatory NPCs was significantly upregulated (**Fig. 1A**). Gene set enrichment analysis (GSEA) further suggests that this process involves the participation of related pathways such as cytokines and chemokines (**Fig. 1B**). We explored expression characteristics of ETS2 in IDD by integrating clinical samples and animal models. Human NP tissues immunohistochemical and WB results showed that expression of ETS2 in severely degenerated human NP tissues was significantly higher than that in mildly degenerated tissues (**Fig. 1D, E; and Supplementary Fig. 1A**). In rat model of intervertebral disc degeneration induced by acupuncture, Safranin O/fast green staining and immunofluorescence confirmed that the degree of degeneration in acupuncture group was significantly more severe than that in sham group, and expression of ETS2 increased simultaneously (**Fig. 1, F and G**). In vitro experiments, we further found that in inflammatory environment induced by TNF-α, expression of ETS2 in NPCs was also upregulated (**Fig. 1H, and Supplementary Fig. 1B**).

In this study, the effects of ETS2 overexpression on NPCs and IDD were systematically elucidated through in vitro and in vivo experiments. In vitro experiments, WB analysis showed that overexpression of ETS2 in NPCs significantly upregulated expression level of anabolic markers ACAN and Collagen II were down-regulated, while expressions of catabolic enzyme matrix metalloproteinase 13 (MMP13) and inflammatory factor TNFR were significantly increased (**Fig. 1C, K and M**). This indicates that overexpression of ETS2 inhibits the anabolic function of NPC, promotes

the catabolic process and intensifies the inflammatory response. In vivo experiments, after in situ overexpression of ETS2 in the tail intervertebral disc of rats, the imaging assessment results showed that after overexpression of ETS2, X-ray and micro-CT detection found a significant decrease in intervertebral disc height index (DHI), and MRI indicated reduction in intervertebral disc water content and significant aggravation of Pfirrmann degeneration grade (**Fig. 1I, L**). The results of HE and Safranin O/fast green staining further indicated that overexpression of ETS2 could lead to significant loss of NP tissue, obvious degradation of proteoglycans, and accompanied by relatively significant fibrosis-like changes (**Fig. 1J**). In conclusion, overexpression of ETS2 disrupts the metabolic balance of NPC and exacerbates inflammation, thereby accelerating the degenerative changes of intervertebral discs on average both in vivo and in vitro.

Inhibition of ETS2 reduces inflammatory response of NPCs and delays IDD progression

In this study, adenovirus knockout technology targeting ETS2 and the ETS2 inhibitor MEKi were respectively employed to intervene in the inflammatory state of NPCs in vitro. RNA sequencing analysis was conducted respectively on the two types of inflammatory NPCs treated above and the inflammatory NPCs that did not receive intervention. The results of GO enrichment analysis showed that differentially expressed genes regulated by the two intervention methods were all co-enriched in biological processes such as protein binding and cell signal transduction (**Fig. 2A, B**). We further explored the regulatory effect relationship of ETS2 in inflammatory microenvironment and functional mechanisms in IDD. In vitro experiments have shown that exogenous addition of TNF-α can significantly up-regulate expression levels of ETS2 in NPCs. On this basis, knocking down ETS2 can effectively inhibit expression of ETS2. In terms of cellular metabolism and inflammatory phenotypes, TNF-α stimulation leads to down-regulation of expression of ACAN and collagen II, and up-regulation of expression of MMP13 and TNFR, thereby inhibiting anabolic metabolism, promoting catabolic metabolism, and intensifying inflammatory responses (**Fig. 2C, E**). It is worth noting that knocking down ETS2 can significantly reverse the

above-mentioned pathological changes induced by TNF-α. In vivo functional assessment further confirmed that compared with the acupuncture group, knocking down ETS2 in the acupuncture degeneration model could significantly improve the intervertebral disc structure. HE and Safranin O/fast green staining showed that in ETS2 knockdown group, the loss of NP tissue was reduced and the degree of fibrosis was significantly alleviated (**Fig. 2F**). X-ray and micro-CT imaging showed a significant recovery in DHI. MRI indicated an increase in the water content of intervertebral disc and a significant decrease in the Pfirrmann degeneration grade (**Fig. 2I, K**). In conclusion, ETS2 plays a key promoting role in inflammation-mediated intervertebral disc degeneration.

Based on the above findings, we further evaluated the therapeutic potential of ETS2 inhibitor MEKi in delaying IDD. In vitro experiments have shown that in the inflammatory microenvironment induced by TNF-α, MEKi can significantly down-regulate expression levels of ETS2. In terms of functional phenotypes, in vitro results indicated that MEKi treatment could up-regulate expression of ACAN and collagen II, while inhibiting expression levels of MMP13 and TNFR (**Fig. 2D, H**). In vivo functional assessment further confirmed that, compared with the simple acupuncture group, the application of MEKi in the acupuncture degeneration model could significantly improve the intervertebral disc structure. The results of HE and Safranin O/fast green staining showed that in MEKi group, the loss of NP tissue was reduced, the degradation degree of proteoglycan was decreased, and the degree of fibrosis was significantly alleviated (**Fig. 2G**). X-ray and micro-CT imaging indicated a significant recovery of DHI. MRI shows an increase in water content of intervertebral disc and a significant decrease in the Pfirrmann degeneration grade (**Fig. 2J, L**). However, CCK-8 results indicated that MEKi has significant cytotoxicity and its safe dose range is relatively narrow (**Fig. 2M**).

Synthesis and characterization of GAC@LTM

To reduce the cytotoxicity of MEKi, broaden its safe dose window and achieve its sustained release in vivo and in vitro,we designed a dual-responsive hydrogel for embedding MEKi. As shown in **Fig. 3A**, we fabricated liposomes modified with DSPE-

TK-PEG-$(OH)_2$ loaded with MEK inhibitors. The specific synthesis steps of DSPE-TK-PEG-$(OH)_2$ are shown in **Supplementary Fig. 2**. HPLC assay confirmed its successful synthesis with very high purity (**Supplementary Fig. 3**). Negative-stain TEM (**Fig. 3B**) corroborates the stepwise construction of liposomal carriers. Blank liposomes (L) exhibit thin, electron-lucent bilayers, whereas DSPE-TK-PEG-modified vesicles (LT) show a moderately thickened contour attributable to the PEG corona. Drug-loaded vesicles (LTM) present a markedly electron-dense core, consistent with successful entrapment of the hydrophobic MEKi. Dynamic-light-scattering data accord with these observations: hydrodynamic diameters rise from 59.5 nm (L) to 74.9 nm (LT) and 79.5 nm (LTM), reflecting both PEGylation and drug incorporation (**Fig. 3C**). Zeta-potential measurements shift from –7 mV (L) to –11 mV for LT and LTM, a change attributable to the anionic phosphate moiety of DSPE that surfaces after PEG conjugation, thereby increasing electrostatic repulsion and colloidal stability (**Fig. 3D, and Supplementary Fig. 4**).

Scanning-electron micrographs (**Fig. 3E, and Supplementary Fig. 5**) reveal that the freeze-processing route governs the internal architecture of GelMA spheres. Microspheres quenched at –20 °C display an almost non-porous, glassy interior, indicating minimal ice-crystal templating. Lowering the temperature to –60 °C and –80 °C produces isolated, micron-scale voids as larger ice nuclei form and are sublimed during lyophilisation. Rapid immersion in liquid nitrogen generates a highly interconnected, open-pore network—a consequence of instantaneous ice nucleation throughout the droplet volume—which markedly increases specific surface area and is expected to enhance both drug loading capacity and subsequent diffusion-controlled release. We used liquid nitrogen quick-freezing to fabricate GelMA microspheres for subsequent experiments. SEM images showed that the groups of microspheres had good porosity, which facilitated cell adhesion and proliferation as well as drug release. In the fractions containing 3-APPBA, EDS scans showed the presence of element B. The EDS scans showed the presence of element B in the fractions containing 3-APPBA. In GAC@L, GAC@LT and GAC@LTM groups, we observed fine particles on the surface of the microspheres in the SEM results, which may be due to the presence of liposomes. EDS scans showed the presence of P element in all the three groups, which

originated from the phospholipids of the liposomes. In the GAC@LTM group, EDS scanning of element S, a disulfide bond in the TK bond, and element I are present in the MEK inhibitor, but in very low amounts (**Fig. 3E, and Supplementary Fig. 6**). The above results corroborate the successful assembly of microsphere liposome complexes. The particle size detection results of each group showed that the average diameter of the microspheres was around 550 micrometers, which was consistent with the SEM images. Microspheres of this size can evade phagocytosis by cells in vivo and exert drug delivery effects for a long time (**Fig. 3F, and Supplementary Fig. 7**).

We then performed an XPS test. The split-peak fits to the assay results for each group are shown in **Fig. 4A** and **Supplementary Fig. 8**. In group G, we obtained C-C, C=O and C-N peaks, which are typical peaks of GelMA. In the GA group, B-O peaks appeared after photopolymerization of GelMA with 3-APPBA. In the GC group, compared to GelMA alone, the C-O peak appeared, originating from citric acid. After microsphere attachment to liposomes, 2p 1/2 and 2p 2/3 peaks appeared in the GAC@L group, which originated from the phospholipids of the liposomes. In the GAC@LT group, the extra S element showed S 2p1/2 and 2p 2/3 peaks, which corroborated the presence of TK bonds. In the GAC@LTM group, compared to the GAC@LT group, the peaks of I 3d 3/2 and 3d 5/2 appeared in the sub-peaks of I element, representing the successful loading of MEKi.

In this study, DSPE-TK-PEG modified on liposome membranes with an o-diol structure at the end could generate a borate bond with the phenylboronic acid moiety. The borate bond allows the microspheres to be tightly attached to the liposomes and breaks in the presence of a decrease in pH. It was demonstrated that the presence of borate bonds is particularly important. Therefore, we performed infrared analysis. As shown in **Fig. 4B**, the peak of group G at 3279 corresponds to the N-H stretching vibration, which is the amino peak of GelMA. 2972 out of the peak corresponds to the C-H stretching vibration, which indicates that GelMA contains both the aliphatic carbon skeleton of gelatin and introduces the alkyl structure of methacryloyl. The peak near 1646 corresponds to the C=O stretching vibration, while the C-N stretching vibration is near 1250. Together, these results confirm the presence of GelMA microspheres. The sharpening of the N-H peak in the GA sample may be due to the addition of 3-AAPBA,

which may have formed a hydrogen bond between the two molecules. This interaction resulted in a more regular restriction of the vibration of the N - H bond and a weakening of the coupling or broadening effect of the vibration, which led to a sharpening of the N-H stretching vibrational peaks, which might otherwise be broadened due to intermolecular interactions. Near 1400, it corresponds to the C=C stretching vibration originating from the benzene ring structure of 3-AAPBA, while the B-O stretching vibration is located near 1100. This confirms the presence of 3-APPBA.The coupling of the hydroxyl peak to the amino peak of the GC group resulted in a broadening of the peak near 3339. A bending vibration of N-H appeared at the original C=O position, which together formed the amide I band, and the peak out near 1250 corresponded to the bending vibration of C-H, which was due to a large number of hydroxyl peaks brought about by the introduction of citric acid. Compared with the GC group, the GAC group had more B-O bonds and wider hydroxyl peaks, which indicated that 3-APPBA was included in the GelMA microspheres together with citric acid. In the GAC@L group, the position of the original hydroxyl group was taken by the carbonyl group of GelMA, and the imino group formed a hydrogen bond with the amino and hydroxyl groups of 3-APBA to enhance the intermolecular bonding, which resulted in a narrower peak shape and an increase in peak intensity. Liposomes are composed of phospholipids (lecithin) and cholesterol, and the surface of the liposome contains phosphate groups, PO42-, amino groups, etc. The peak of P=O is near 1050. The phosphate group of phospholipids can form an electrostatic interaction with the amino group of GelMA, and the ester group can bind to the benzene ring of 3-AAPBA by van der Waals forces. The liposomes regulate the phase behavior and biocompatibility of the system through the above interactions. The GAC microspheres were shown to adsorb certain liposomes.The peak out of P-O in the GAC@LT group was located near 1100, which was mainly from phospholipids in the liposomes. The peak near 1050 indicates the formation of borate bond, which was generated by the reaction of the phenylboronic acid group of 3-AAPBA with the terminal o-diol structure of DSPE-TK-PEG-OH_2, confirming the formation of the covalent bond in the GAC@LT group, suggesting that the microspheres and the liposomes were successfully connected by the borate bond. GAC@LTM due to the addition of an iodine-containing MEK inhibitor. C-I also

appeared near 872, originating from the carbon iodine single bond stretching vibration in the added MEK inhibitor, proving that the MEK inhibitor had been successfully introduced into the system.

And then the transmission FTIR spectra of each group were analyzed for 2D correlation. The 2D correlation analysis was firstly plotted using 2D Shige software and then plotted as contour plots using Origin2019b software (**Fig. 4E, F**). The key of this study is the change of borate bond, and since the characteristic peaks of borate bond in the infrared spectra come out in the range of 900-1400 cm-1, the wave number of 900-1400 cm-1 was selected for the 2D infrared correlation analysis. In the 2D spectrum, the red region is the positive correlation peak and the blue region is the negative correlation peak. According to Noda's 2D correlation spectral theory, Φ (υ1, υ2) and Ψ (υ1, υ2) are the cross-peak signals in the 2D correlation synchronous and asynchronous spectra, respectively, and υ1 and υ2 are two sets of correlated IR absorption peaks. A positive cross peak in the synchronous spectrum indicates that the two correlation peaks change in the same direction, and vice versa. If Φ (υ1, υ2) and Ψ (υ1, υ2) have the same sign, i.e., the same positive correlation peaks or the same negative correlation peaks, then the change of υ1 is prioritized over υ2, which is denoted by υ1 > υ2, and vice versa, if the signs of Φ (υ1, υ2) and Ψ (υ1, υ2) are opposite, then the change of υ1 lags behind υ2, which is denoted by υ1 < υ2. In addition, if Φ (υ1, υ2) is a positively correlated peak or a negatively correlated peak, and Ψ (υ1, υ2) has no signal, then υ1 and υ2 change at the same time, which is denoted by υ1 = υ2, and vice versa, it is not possible to determine the order of υ1 and υ2 changes.

In the two-dimensional infrared synchronogram, the auto peaks near Φ (952, 1100) are green and positive, indicating that the dynamic fluctuations of these vibrational modes themselves are more significant, indicating the existence of intermolecular interactions, and Φ (952, 1050) is also green and positive, indicating that the two related peaks change in the same direction, and the changes of the functional groups are in the same direction, reflecting that the two are changing synchronously, and are simultaneously enhanced or diminished, and in the asynchronous plot, Ψ (952, 1100) is also green and positive, which indicates that 952 and 1100 are the same positively correlated peaks, and the change at 952 cm-1 is prioritized over that at 1100 cm-1, in

which the 952 cm-1 peak is attributed to the methacryloyl=C-H out-of-plane bending vibrational peak in GelMA, and the 1100 cm-1 peak is the C-O-C asymmetric C-O-C asymmetrical C-O-C vibrational C-O-C asymmetric C-O-C vibrational C-O-C asymmetric C-O-C vibration of methacrylate groups. The 1100 cm-1 peak is the C-O-C asymmetric stretching vibration of the methacrylate group, and there is a synergistic variation of these two vibrational modes in the GelMA network. 3-AAPBA introduced into the borate bond enhances the intensity of the 952 cm-1 and 1100 cm-1 peaks. The synchronized peaks were positive indicating that the B-OH stretching vibration peaks appeared after the introduction of 3-AAPBA. In GelMA+citric acid, the carboxyl group of citric acid may affect the C-O-C vibration of the methacrylate group through hydrogen bonding or electrostatic interactions, which makes the synchronized change with the methacrylate group, and the B-OH of 3-AAPBA changed in synchrony with the methacrylate group after the simultaneous addition of citric acid and 3-AAPBA to the GelMA. OH and the hydrogen bonding network of the citric acid carboxyl group acted together and hydrogen bonding occurred, leading to the superposition of the intensity of the two peaks to enhance the intensity of the two peaks, and after continuing to add liposomes, the hydrophobic microenvironment of liposomes could enhance the symmetric telescopic vibration of the B-OH through the spatial site-barrier; and then after adding the DSPE-TK-PEG-(OH)2, the breakage of the TK bond led to the detachment of the PEG chain, which disrupted the hydrogen bonding interaction of the B-OH and made the vibrational mode to change . Reflecting the synchronization between B-OH bond breaking and vibrational mode change, a new B-O-C borate bond was formed. Finally, after the addition of MEK inhibitor, the MEK inhibitor affects the coordination environment of the borate bond through hydrogen bonding and π-π stacking, resulting in the change of peak intensity, which can interfere with the coordination of the borate bond with citric acid and change the hydrogen bonding network of the substrate, and the interaction between the inhibitor and the borate bond is synchronized with a certain degree of interference. In addition, the peaks near Φ (1100, 1050) in the two-dimensional synchronous diagram are also positively correlated, and Ψ (1100, 1050) in the asynchronous diagram is also positively correlated, which are attributed to the C-O-C vibration of the PEG chain and the B-O-C vibration of the

boronate bond, respectively, and the synergistic change of the two (positively synchronous peaks) reflects the interactions between the PEG chain and the boronate bond; and the asynchronous peaks are positively correlated, which reflects the different The positive asynchronous peak reflects the kinetic difference between the different vibrational modes. In the DSPE-TK-PEG-OH2-containing material, the changes of the borate bond are mainly regulated by the spatial resistance of the PEG chains and the breaking of the TK bond: the unstimulated PEG chains restrict the vibration, and the detachment of the PEG leads to the enhancement of the vibration and the stabilization of the structure after the stimulation, which further confirmed the formation of the borate bond.

Degradation profiles of the GAC@LTM composite (**Fig. 4C**) reveal a biphasic mass-loss pattern—rapid erosion within the first 48 h followed by a decelerated phase—across all media tested. In collagenase-supplemented PBS (pH 7.4) the matrix is most stable, underscoring the inherent resistance of highly cross-linked GelMA to neutral hydrolysis. Mild acidification to pH 5.5 accelerates breakdown only modestly; protonation of boronate esters promotes partial liposome detachment, yet the negligible mass of the freed vesicles means overall degradation increases only slightly. Under oxidative stress (100 μM H_2O_2, pH 7.4) APBA units undergo partial oxidation to phenolic species, further loosening the network and shortening the completion time to ≈10 d. The combined acid/ROS condition exerts a synergistic effect, producing the fastest erosion owing to concurrent boronate cleavage and APBA oxidation. Release kinetics mirror these degradation trends (**Fig. 4D, and Supplementary Fig. 9**). Citric-acid liberation tracks matrix erosion, attaining about 80 % cumulative release between day 6 and day 8, suggesting that diffusion through the expanding pore network rather than burst leaching dominates transport. In contrast, Mirdametinib release is governed by liposome integrity. In physiological PBS, the carrier is highly stable, and only about 35 % of the drug is liberated within 72 h. Acidic pH breaks boronate linkages, freeing vesicles from the GelMA surface; consequently about 55 % release is observed over the same period. High ROS levels cleave thioketal linkers within the lipid corona, rupturing vesicles and producing a dramatic surge— about 80 % release within 24 h. These data confirm the dual-responsive design: early, ROS-triggered delivery of the

anti-inflammatory MEK inhibitor can rapidly modulate macrophage phenotype, whereas the sustained citric-acid release supplies metabolic intermediates to surrounding cells during later regenerative phases.

Biocompatibility of the GAC hydrogel

As a therapeutic vehicle implanted in vivo, biocompatibility is the primary prerequisite for clinical application. In this study, the biosafety of GAC@LTM was systematically evaluated through a rigorous in vitro and in vivo experimental system. Live/Dead fluorescent staining visualizes the survival state of NPCs in the presence of GAC@LTM. The staining results showed that the vast majority of cells showed green fluorescence (live cells) and a very small number of dead cells (red fluorescence), and there was no significant difference from the control group (**Supplementary Fig. 10A, B**). This directly confirmed that the components of GAC@LTM had no adverse effect on the activity of NPCs under in vitro conditions, and had a good basis for cytocompatibility. The CCK-8 method was used to detect the cell viability of GAC@LTM co-cultured with NPCs. The results showed that, compared with the control group, the activity of NPCs in the GAC@LTM treatment group was not significantly inhibited, and showed a certain trend of promoting proliferation, indicating that the GAC@LTM itself and its degradation products were not cytotoxic to NPCs, and were even conducive to maintaining cell activity and growth (**Supplementary Fig. 10C**). After the application of GAC@LTM to rats, histopathological analysis was performed on the main organs like heart, liver, spleen, lungs, and kidneys. The results of HE staining showed that the structure of each organ and tissue was clear and complete, and no obvious pathological changes such as inflammatory cell infiltration, hyperemia, edema, degeneration or necrosis were observed. This indicates that after the application of GAC@LTM in vivo, it does not produce acute or subacute toxic effects on major living organs (**Supplementary Fig. 11A**). Excellent in vivo biosafety hemocompatibility is a key index to evaluate the safety of biomaterials in contact with blood. The results of in vitro hemolysis experiments of GAC@LTM showed that after contact with red blood cells, it did not cause obvious hemolysis, and the hemolysis rate was much lower than the international

standard (usually <5%) (**Supplementary Fig. 11B**). This proves that GAC@LTM does not disrupt the red blood cell membrane structure, has good hemocompatibility, and reduces the risk of triggering thrombosis or systemic inflammatory reactions after implantation. The results of live/dead staining, CCK8 and in vivo organ toxicity and hemolysis experiments fully confirmed that the pH/ROS dual-responsive GAC@LTM has good biocompatibility, which lays a solid foundation for its safe application as an intradiscal drug delivery vehicle and therapeutic agent.

In vitro validation of the anti-inflammatory and anti-oxidant effects of GAC@LTM hydrogel

Chronic inflammation is the core pathological link driving the progression of IDD, which is characterized by a large release of inflammatory factors, inhibition of matrix synthesis and hypercatabolism. In this study, TNF-α was used to stimulate NPCs to construct an in vitro inflammation model, and the anti-inflammatory efficacy of GAC@LTM and its regulatory role in extracellular matrix (ECM) homeostasis were deeply explored. Immunofluorescence staining and WB showed that expression level of ETS2 was low in normal NPCs. After stimulation by TNF-α, ETS2 expression was significantly up-regulated, which was consistent with the performance of degenerative NP tissue in vivo. After the intervention of GAC@LTM, the TNF-α-induced ETS2 overexpression could be effectively reversed, and its fluorescence intensity was significantly reduced (**Fig. 5A, B and J**), what it suggests about GAC@LTM can target key inflammatory signaling that inhibit aberrant activation in IDD. ECM, especially ACAN and Collagen II, is central to maintaining the hydration and mechanical function of the NP tissue of the intervertebral disc. WB and immunofluorescence showed that TNF-α stimulation led to a significant decrease in the ability of NPCs to synthesize ACAN and Collagen II. GAC@LTM reprogram reversed this trend and significantly increased expression levels of these two key matrix components (**Fig5. J, and Supplementary Fig. 12A, B**). During the progress of IDD, overexpression of MMP13 is a key factor leading to ECM degradation disruption. The results of immunofluorescence and WB showed that expression of MMP13 in NPCs was significantly increased after TNF-α stimulation. The application of GAC@LTM can

significantly downregulate expression of this catabolic enzyme and effectively protect ECM from damage (**Fig. 5C, D and J**). In an in vitro model of inflammation, GAC@LTM demonstrated strong anti-inflammatory and matrix regenerative abilities, and reversed inflammation-induced NPCs dysfunction and ECM metabolic imbalance.

Oxidative stress and the cellular senescence caused by it are another important pathological mechanism for the occurrence and development of IDD. We evaluated the efficacy of GAC@LTM in scavenging ROS and fighting cellular senescence. In TNF-α-induced in vitro model, DCFH-DA fluorescent probe method showed a significant increase in ROS levels in NPCs. After the intervention of GAC@LTM, it can effectively reduce the fluorescence intensity of intracellular ROS (**Fig. 5E, F**), indicating that it has a good ability to directly remove ROS and enhance cellular antioxidant defense, and can reduce oxidative damage in inflammatory environment. β-galactosidase (SA-β-gal) is a signature enzyme for cellular senescence. The results of SA-β-gal staining showed that TNF-α stimulation led to a significant increase in the proportion of SA-β-gal positive cells in NPCs. However, GAC@LTM reprogram can significantly reduce the rate of SA-β-gal-positive cells, which proves that it has effect of resisting inflammation-induced cell senescence (**Fig. 5G, H**). The p53-p21-RB pathway is a core signaling axis that regulates cellular senescence [36]. Both immunofluorescence and Western blot results showed that expression of cell cycle inhibitory protein p21 in NPCs was significantly increased under TNF-α stimulation. The application of GAC@LTM can significantly reduce the protein expression level of p21, but has no obvious effect on the protein expression level of p16 (**Fig. 5I, J**). GAC@LTM exhibits significant anti-oxidative stress and anti-cellular senescence effects in an in vitro inflammatory model. It directly removes excess ROS in NPCs, reduces secondary matrix degradation and ROS production, and protects NPCs from oxidative stress-induced dysfunction, matrix degradation and senescence (**Fig. 5K**).

RNA sequencing reveals potential pathways for GAC@LTM to play therapeutic role

In order to further elucidate the molecular mechanism of GAC@LTM in alleviating IDD, high-throughput RNA-seq was performed on NPCs treated with GAC@LTM and

with GelMA under the intervention of TNF-α to analyze the core pathways and key molecules focusing on the regulation of GAC@LTM. Kyoto encyclopedia of genes and genomes (KEGG) enrichment analysis demonstrated that GAC@LTM exerts its therapeutic effect by modulating TNF signaling pathway, MAPK signaling pathway and IL-17 signaling pathway (**Fig. 6A**). To further demonstrate the attribution and co-occurrence relationship between core genes and significant enrichment pathways, we used enrichment string plots to visualize the enrichment results. The analysis revealed that the genes were predominantly clustered in pathways related to cell signal transduction, inflammation and ECM. Specifically, expression of genes associated with inflammation, such as *Ptgs2*, *Cxcl2* and *Cxcl3* and genes involved in ECM degradation, including *Mmp3* and *Mmp9* was notably decreased. At the pathway level, there may be complex regulatory network intersections and mutual interference among the three pathways. At the genetic level, both *c-Jun* and *Ikbkb* are simultaneously associated with three pathways, presenting typical characteristics of "hub genes", suggesting that they may play a core role in the coordinated regulation of multiple pathways (**Fig. 6B**). Studies have reported that ETS2 can specifically bind to c-Jun, but the downstream signaling mechanism remains to be clarified [18].

We then deeply clarified the molecular interaction mechanism and regulatory network of ETS2 and c-Jun in NPCs. Firstly, co-immunoprecipitation (Co-IP) experiment confirmed that there was endogenous physical binding between ETS2 and c-Jun in NPCs (**Fig. 6C**). However, exogenous TNF-α stimulation cannot significantly enhance the binding strength between the two (**Fig. 6D, K**). Secondly, WB showed that after overexpression of ETS2, the expression level of c-Jun increased accordingly (**Fig. 6F, L**). After knocking down ETS2 in inflammatory environment, the expression of c-Jun also decreased accordingly (**Fig. 6G, M**). In addition, the application of MEKi in inflammatory environment can also significantly down-regulate the expression level of c-Jun (**Fig. 6C, H and N**). The above results suggest that there is a positive regulatory relationship between ETS2 and c-Jun. Meanwhile, a luciferase reporter plasmid containing the 2kb proximal c-Jun promoter showed a positive response to ETS2 overexpression, suggesting that ETS2 directly targeted and positively regulated c-Jun (**Fig. 6I**). c-Jun ablation also augmented chondral production (ACAN and Collagen II)

and suppressed catabolism (MMP13) and inflammation (TNFR) after ETS2 overexpression in rat NPCs (**Fig. 6J**). Collectively, ETS2 directly targets c-Jun to induce metabolic imbalance and inflammation in rat NPCs.

On this basis, we further analyzed functional regulatory relationship of ETS2/c-Jun axis: overexpression of ETS2 not only upregulates expression of c-Jun, but also leads to inhibition of anabolism, enhancement of catabolism and intensification of inflammatory response. Conversely, knocking down c-Jun can effectively reverse the above pathological phenotypes, manifested as promoting anabolism, inhibiting catabolism and reducing inflammatory responses. In summary, ETS2 positively regulates c-Jun through direct transcriptional activation, thereby mediating the metabolic imbalance and inflammatory process of NPC.

GAC@LTM enhanced NP regeneration *in vivo*

In vivo efficacy evaluation is a key link in verifying the therapeutic potential of GAC@LTM. In this study, a rat caudal intervertebral disc acupuncture IDD model was used to evaluate the structural repair effect of intervertebral discs through a variety of imaging and histological methods (**Fig. 7A**). Plain x-rays are a routine means of assessing disc height. The discs at 4 weeks after acupuncture modeling were examined by X-ray and micro-CT and DHI was calculated. The results showed that DHI was significantly reduced in IDD group, indicating disc height loss (**Fig. 7B, C**). The DHI value of the intervertebral disc treated with local injection of GAC@LTM was significantly higher than that of the IDD group. This intuitively proves that GAC@LTM can effectively restore the lost height of the degenerated disc and maintain the normal spatial structure of the disc. MRI is the gold standard for assessing the degree of disc degeneration, particularly the NP hydration status and structure. The Pfirrmann grading system was used to analyze MR images, usually T2-weighted images. The results showed that the Pfirrmann grade of the intervertebral disc in the IDD group was significantly increased, which was manifested by reduced signal intensity, height loss, and structural disturbance. The Pfirrmann grade of the intervertebral disc in the treatment group was significantly lower than that in the IDD group, indicating that the water content and signal intensity of the NP tissue were partially restored and the degree

of degeneration was reduced (**Fig. 7B, D**).

Subsequently, we collected intervertebral disc specimens, prepared pathological sections, and performed histological staining. The results of blood biochemical tests are shown in **Fig. 7I**. Histological analysis is the most direct evidence to evaluate the effect of IDD repair by directly observing the changes in the tissue structure, cell morphology and matrix composition of the intervertebral disc at the microscopic level. HE staining assesses overall tissue structure and cell morphology. Normal NP tissue is rich in chondrocytes and is distributed in a rich basophilic matrix with clear demarcation. The IDD group showed that the NP area was significantly reduced or even disappeared, and was invaded by fibrous tissue. Decreased number of NPCs and abnormal tissue morphology were also observed. The NP is indistinctly demarcated from the annulus fibrous. The histological structure of the NP in the GAC@LTM treatment group was significantly improved. The NP area was larger than that in the IDD group. Number of NPCs increased and NP tissue was nearer to normal morphology. Degree of organizational disorder reduced and NP-annulus fibrous demarcation was clear. Assessed using a standard histological grading system, the score in the GAC@LTM treatment group was significantly lower than that in the IDD group. Safranin O/Fast Green staining specifically assesses the content and distribution of proteoglycans. The normal NP is rich in proteoglycans and is strong Safranin O positive. In the IDD group, the staining intensity of Safranin O was significantly weakened, indicating that the proteoglycan was seriously lost. The staining intensity of Safranin O in the NP tissue of the GAC@LTM treatment group was significantly higher than that of the IDD group, indicating that the proteoglycan content was effectively restored and maintained. Collagen distribution also tended to normalize. Histological scoring also confirmed that GAC@LTM significantly improved the matrix composition of the degenerative disc (**Fig. 7E, J**). IHC and IF were used to detect the key matrix components Collagen II and ACAN. Expression of Collagen II and ACAN in the NP of the IDD group was significantly reduced. Expression levels of these two matrix proteins in GAC@LTM treatment group were significantly higher than those in IDD group, which directly confirmed that GAC@LTM promoted the recovery of anabolism in the degenerated disc matrix in vivo (**Fig. 7F, K, H and L**). IHC detected matrix catabolic enzyme

MMP13 which primarily degrades Collagen II. Expression of MMP13 in NP of IDD group was significantly increased. Expression level of MMP13 in GAC@LTM treatment group was significantly lower than that in the IDD group, indicating that GAC@LTM effectively inhibited the excessive decomposition and destruction of the intervertebral disc matrix in vivo (**Fig. 7G, K**). Histological evaluation provides the most direct evidence that GAC@LTM promotes IDD regeneration at the microscopic level. It significantly improves the tissue structure of degenerated discs, restores the NP area, and increases the number of cells in normal morphology, and effectively restores the content and distribution of proteoglycan and collagen II in NP tissue. At the molecular level, expression of anabolic markers like ACAN and Collagen II was significantly upregulated, and expression of MMP13, a key catabolism enzyme, was significantly downregulated. These results corroborate each other with in vitro experimental results and imaging results, and jointly establish the strong ability of GAC@LTM to achieve structural repair and functional regeneration of intervertebral discs by remodeling the homeostasis of ECM.

Discussion

IDD is the main cause of lower back pain, imposing a heavy socio-economic burden on the global public health system [37]. The current clinical treatment methods for IDD mainly include conservative treatment and surgical intervention [38]. The former can only relieve symptoms, while the latter, although it can relieve nerve compression, cannot reverse the biological process of degeneration [39,40]. Therefore, clarifying the pathogenesis of IDD at the molecular mechanism level and developing new therapeutic strategies that can repair the IDD process based on this is the research focus and difficulty in this field. This study identified ETS2 as a novel IDD marker molecule for the first time in human clinical NP specimens and rat caudal vertebra acupuncture models. Its expression level was significantly increased in degenerated NP tissues. Further mechanism studies have shown that ETS2 up-regulates the expression of c-Jun through transcription, thereby activating the downstream inflammatory cascade reaction. Specifically, it promotes the expression of the inflammatory factor receptor TNFR, enhances the expression of the catabolic marker MMP13, and simultaneously

inhibits the expression of anabolic markers ACAN and Collagen II. In both in vivo and in vitro experiments, overexpression of ETS2 can induce typical degenerative phenotypes, including decreased intervertebral disc height, elevated Pfirrmann grade, reduced water content, and degradation of nucleus pulposus tissue. However, knockdown of ETS2 or application of MEKi can effectively reverse the above degenerative effects. Given the significant systemic toxicity risk of MEKi itself, in this study, a dual-responsive hydrogel GAC@LTM was further designed and constructed. Antioxidant citric acid was embedded in the GelMA skeleton, and a composite structure of APBA and liposomes was grafted on the outer layer. The liposomes were cross-linked with DSPE-TK-PEG-$(OH)_2$ and embedded with MEKi. The spatio-temporal controlled release of drugs is achieved by taking advantage of the pH response of borate ester bonds and the ROS response characteristics of TK bonds, which significantly reduces drug toxicity while stabilizing and enhancing therapeutic effects.

ETS2, a prototypical member of the ETS transcription factor family, plays critical regulatory roles in inflammatory diseases, cell proliferation, and differentiation [10,41]. However, the function of ETS2 in the field of IDD has rarely been reported. One of breakthrough findings of this study is the first demonstration, through cross-validation using human clinical NP specimens and a rat caudal disc puncture-induced degeneration model, that ETS2 is significantly upregulated in degenerated NP tissue, suggesting that ETS2 may serve as a potential biomarker and therapeutic target for IDD. This pathological function of ETS2 in IDD is not an isolated tissue-specific phenomenon. Research has found that ETS2 also plays a key role in degenerative and inflammatory diseases of other musculoskeletal systems. Studies have reported that in patients with rheumatoid arthritis, ETS2 mediates osteoclast-like transformation of synovial fibroblasts induced by IL-6 cross-signal transduction [42]. The expression and nuclear translocation of ETS2 are positively correlated with the expression of RANKL, cathepsin B and K, suggesting that ETS2 is a hub transcription factor that can be activated by multiple inflammatory signals [42]. In the research of osteoarthritis, ETS2 regulates osteoclast differentiation by targeting and enhancing the expression of CEBPB. Knockdown of ETS2 can alleviate subchondral bone remodeling and the progression of osteoarthritis in DMM model mice [43].

This study found that TNF-α activated ETS2, and ETS2 further transcriptively upregulated c-Jun, constituting the positive drive axis of TNF/ETS2/c-Jun. TNF-α, as a key pro-inflammatory cytokine, has been confirmed by numerous studies to be the core driving factor for the initiation and progression of IDD [44]. TNF-α derived from NPCs themselves can trigger the NF-κB pathway to participate in the degeneration process [45]. This study fills the gap of specific transcriptional mediator molecules in NPCs between TNF signaling and downstream AP-1 activation. Studies have confirmed that c-Jun and NF-κB are activated in the process of human IDD [46,47]. Inhibiting NF-κB can eliminate the catabolic effect of IL-1β to the greatest extent [48]. In this study, ETS2 was placed at the key node position between TNF and c-Jun, providing a brand-new explanation for understanding the inflammatory cascade signal of IDD.

NPCs are the core cell population that maintains the intact structure and function of intervertebral discs. The dynamic balance between their anabolism and catabolism is the key to determining the health status of intervertebral discs. This study clearly Outlines the multi-level effects of the ETS2/c-Jun axis-driven NPCs degeneration. Firstly, at the ECM metabolic regulation level, overexpression of ETS2 leads to a significant downregulation of anabolic markers ACAN and Collagen II, while inducing an upregulation of catabolic marker MMP13. The pathogenic effect of MMP13 in IDD has been relatively fully verified [49]. Its elevated expression can accelerate the degradation of ACAN and Collagen II in the extracellular matrix, resulting in irreversible matrix destruction [50,51]. This study reveals that the activation of the ETS2/c-Jun axis is directly involved in the matrix catabolism process of NPCs. Secondly, at the level of inflammatory response remodeling, NPCs with ETS2 overexpression show a significant increase in the expression level of the inflammatory factor receptor TNFR. The upregulation of TNFR is not a direct expression of inflammatory mediators, but rather amplifies the sensitivity of the NP microenvironment to inflammatory signals such as TNF-α [52]. TNF-α can positively feedback regulate XBP1 to promote the proliferation of NPCs through the NF-κB pathway, but it is also involved in inflammation-induced catabolism [53,54]. The upregulation of TNFR observed in this study indicates that NPCs with overexpressed ETS2 are more inclined to respond more strongly and persistently to the surrounding inflammatory signals, thus forming a

vicious cycle of inflammation and ECM destruction. Thirdly, knockdown of ETS2 in vivo and in vitro or application of MEKi could reverse all the above-mentioned degenerative phenotypes, including restoring the expression of ACAN and Collagen II, reducing MMP13 levels, improving intervertebral disc height and water content. This stereoscopically verified the pathogenic role of the ETS2/c-Jun axis in IDD from both functional acquisition and functional loss perspectives, and also provided logical basis for subsequent therapeutic strategies targeting this pathway.

P21 is a cell cyclin-dependent kinase inhibitor and a classic marker of cellular senescence, serving as the ultimate executor of the p53-dependent senescence pathway [55,56]. This study suggests that the expression of p21 is inhibited after targeting ETS2, which implies that the ETS2/c-Jun axis may not only affect the inflammatory and matrix metabolic programs of NPCs, but also be involved in the regulation of cellular senescence fate. In recent years, cellular senescence has been regarded as one of the core driving mechanisms of the IDD process [57]. The senescent NPCs accumulated in the degenerating intervertebral disc tissue exhibit typical senescence-associated secretory phenotype (SASP), which in turn exacerbate the deterioration of the microenvironment by releasing various inflammatory factors and matrix proteases [58]. Studies have confirmed that ROS can induce premature aging of NPCs by activating the p53-p21-Rb pathway through DNA damage [59]. In this study, the use of GAC@LTM hydrogel effectively reduced ROS levels and decreased the number of SA-β-gal positive cells. In other words, the ETS2/c-Jun axis may have promoted the senescence phenotype of NPCs through the ROS-p21 signaling pathway, while the dual-response hydrogel cleared ROS and thus disrupted this signaling chain, achieving an anti-aging effect. Meanwhile, studies have reported that Sirt2 can inhibit oxidative stress and NPCs senescence by suppressing the p53/p21 pathway, further confirming the pivotal position of the ROS-p53-p21 pathway in the regulation of NPCs senescence [59–61]. The accumulation of senescent cells themselves will continuously stimulate the surrounding microenvironment in the form of SASP, intensifying the driving effect of the ETS2/c-Jun axis. The hydrogel in this study, by reducing ROS levels and down-regulating p21 expression, synergistically alleviate the inflammatory burden related to aging from two dimensions: inhibiting the initiation of cellular senescence and eliminating existing

senescent cells.

GelMA is a photosensitive biological material formed by the chemical reaction polymerization of gelatin and methacrylate anhydride at 50 °C [62]. It features excellent biocompatibility and adjustable mechanical properties, and has been widely used in the tissue engineering treatment of IDD [62–64]. In this study, GelMA was selected as the skeleton material to encapsulate CA and construct the core support structure of the hydrogel system. From the perspective of biocompatibility, the degradation products of GelMA are fragments of natural gelatin derivatives and do not cause obvious local or systemic immune rejection reactions [65,66]. In fact, studies have reported that GelMA hydrogels loaded with KGN and IL-10 can effectively alleviate the progression of degeneration and promote the regeneration of NP tissues in needle-induced IDD models [67,68]. The design concept of embedding CA in this study is in line with the above-mentioned strategy of integrating natural antioxidants into GelMA. From the perspective of physical and chemical properties, the injection performance of GelMA enables it to be precisely delivered to the intervertebral disc target area through minimally invasive methods [67]. In this study, the GelMA skeleton forms a stable three-dimensional network structure under physiological conditions [69]. On the one hand, it provides a physical barrier for the sustained release of CA; on the other hand, its internal pore structure allows for the diffusion and exchange of small molecules in the microenvironment [70,71]. More importantly, GelMA has excellent potential for double crosslinking modification [72]. The APBA coating used in this study was achieved through surface functionalization treatment of the GelMA skeleton [65]. The phenylboronic acid group on APBA can undergo a specific condensation reaction with the o-diol structure on the DSPE-TK-PEG-$(OH)_2$ molecule modified on the outer layer of liposomes, forming a dynamic and reversible boronic acid ester bond [73]. Multiple studies have confirmed that the hydrogel system modified with phenylboronic acid can effectively achieve a ROS-responsive drug release mode and be used in the treatment of central nervous system injuries and osteoarthritis [74,75].

The pathological microenvironment of IDD has two significant characteristics: decreased local pH and elevated ROS levels [76]. Due to the accumulation of lactic acid, a metabolic product of anaerobic glycolysis, in the degenerated intervertebral disc, the

pH value of the microenvironment drops from approximately 7.4 under physiological conditions to approximately 6.5-6.8 [77]. At the same time, mitochondrial dysfunction and inflammatory response activation generate a large amount of reactive oxygen species such as superoxide anions and hydrogen peroxide, significantly increasing the level of ROS [78]. The GAC@LTM hydrogel designed in this study is precisely a dual-response system that fits the characteristics of these two microenvironments. Borate ester bonds are typical PH-responsive chemical bonds [79]. The borate ester bond formed by phenylboronic acid and o-diol remains stable under neutral or alkaline pH conditions, while under acidic conditions, the borate ester bond can undergo reversible hydrolysis and cleavage [80]. When the GAC@LTM hydrogel is injected into the degenerated intervertebral disc, the local acidic environment triggers the dissociation of the borate ester bond between APBA and DSPE-TK-PEG-$(OH)_2$, and the liposomes are released from the surface of the hydrogel. This enables MEKi to be unlocked from the system, initiating the drug release procedure [81]. Previous studies have designed phenylboronic acid-modified nanoparticles for osteoarthritis and dynamic double-cross-linked hydrogel systems for IDD by utilizing a mechanism similar to pH response [80]. The DSPE-TK-PEG-$(OH)_2$ molecule inserted on the surface of liposomes contains a crucial TK bond [82]. The TK bond can be specifically cleaved by high concentrations of ROS [83]. The cleavage mechanism is that ROS oxidizes sulfur atoms to form sulfoxides or sulfone intermediates, and then breaks the carbon-sulfur bond through intramolecular cyclization or hydrolysis [84]. ROS-responsive hydrogels are used in the treatment of various diseases such as spinal cord injuries and osteoarthritis [83]. Studies have applied ROS-degradable hydrogels to deliver LOXL2-LNPs, simultaneously inhibiting the senescence and oxidative damage of NPCs, demonstrating promising therapeutic prospects [85]. In this study, the TK bond was introduced into the liposome coating, achieving precise drug release driven by ROS. Only when the ROS concentration in the microenvironment exceeded the threshold did the liposome structure disintegrate and release the internally embedded MEKi, thereby realizing the real-time matching of drug release and inflammatory oxidation levels. The innovation of this study lies in integrating the pH response (borate ester bond) and the ROS response (TK bond) into a single drug delivery system, forming a sequent-dependent triggering mechanism.

Firstly, under the action of the acidic pH in the degenerated microenvironment, the borate ester bond dissociates, allowing the liposome to be released from the hydrogel. Subsequently, after the liposomes are internalized by NPCs, the TK bond breaks in the cytoplasmic environment with high ROS levels, and the MEKi is precisely released around the nucleus to exert its function, ensuring that the drug is released at the correct time and location. At the same time, it greatly reduces the exposure of the drug to non-pathological tissues and non-pathological periods, thereby lowering the systemic toxicity risk of the MEKi.

MEKi is a class of small molecule compounds targeting the Ras/Raf/MEK/ERK signaling pathway and has been widely used in the clinical treatment of malignant tumors such as melanoma and non-small cell lung cancer [86]. However, its clinical application is limited by severe toxic and side effects [86]. The hydrogel strategy used in this study provides a promising improvement scheme for the toxicity of MEKi. In vitro experiments confirmed that there was no significant effect on cell activity after treatment with GAC@LTM hydrogel, no abnormalities were found in organ toxicity tests, and no systemic hemolytic reaction was triggered. These safety indicators are not only attributed to the improvement of the administration method from systemic administration to local delivery, but also to the effective regulation of the multi-level sustained-release mechanism in the hydrogel system. In addition, in recent years, some people have designed MEKi derivatives with rapid systemic metabolic characteristics (NFX-179) to reduce systemic toxicity outside the skin [87,88]. Compared with the molecular structure modification strategy, the advantage of the hydrogel strategy in this study lies in that it does not change the structure and pharmacological activity of MEKi itself. It only reduces its off-target toxicity through the encapsulation and targeted release mechanism of biomaterials, and better retains the efficacy of MEKi as an upstream kinase inhibitor targeting the ETS2/c-Jun axis.

The functional regeneration exhibited by GAC@LTM in vivo has important clinical translational value. Radiologically, it restored DHI and Pfirrmann grading, histologically demonstrated ACAN and Collagen II regeneration, and promoted NP tissue regeneration. These changes not only reverse structural degeneration, but also rebuild the mechanical bearing and shock absorption function of intervertebral disc. Its

injectable nature makes it suitable for minimally invasive interventions, while its dual-response design ensures safety and targeting of treatment.

There are several limitations to this study. Firstly, the downstream molecular target map of the ETS2/c-Jun signaling axis is still incomplete. This study mainly focused on representative markers such as ACAN, Collagen II, MMP13 and TNFR, but failed to systematically identify the transcriptional regulatory network of ETS2 at the whole-genome level in NPCs. Secondly, the diagnostic value of ETS2 as a clinical marker has not yet been prospectively verified. This study only detected the increase of ETS2 in clinical degeneration specimens, but did not analyze the quantitative correlation between the expression level of ETS2 and clinical parameters such as Pfirrmann grade, intervertebral disc water content, and pain score.

In this study, an injectable hydrogel with good biocompatibility, pH and ROS dual-responsiveness was developed. The hydrogel can be locally injected into degenerative NP tissues, releasing anti-inflammatory drugs and antioxidants locally, achieving anti-inflammatory and ECM regeneration effects, and successfully applied to IDD treatment. In addition, RNA sequencing elucidated that TNF/ETS2/c-Jun signaling pathway is specifically involved in IDD therapy. Therefore, we believe that this dual-responsive injectable hydrogel holds great promise in the early treatment of IDD to prevent the development of lumbar degenerative disease.

Materials and methods

Ethics statement

All animal experiments were conducted in accordance with the guidelines approved by the Institutional Animal Care and Use Committee (IACUC) of the Second Affiliated Hospital of Soochow University (Jiangsu, China). Experimental procedures strictly adhered to the Animal Research: Reporting of In Vivo Experiments (ARRIVE) guidelines, and all efforts were made to reduce animal suffering and minimize discomfort throughout the study. Human intervertebral disc specimens were collected following approval from the Institutional Review Board (IRB) of the Second Affiliated Hospital of Soochow University, Jiangsu, China. Written informed consent was obtained from all participants prior to sample collection (Permission number: JD-LK-

2019-080-01).

Preparation of bi-responsive microsphere liposome complexes

Five grams of Type A porcine gelatin were dissolved in 50 mL of pre-warmed PBS (50 °C) under continuous stirring until a clear solution was obtained. Methacrylic anhydride (4 mL) was then added drop-wise at 0.5 mL min^{-1} while maintaining the temperature at 50 °C, and the reaction was allowed to proceed for 2 h; the pH was continuously adjusted to 8.0 ± 0.1 to minimise gelatin backbone degradation. The reaction was quenched by diluting the mixture with an equal volume of 37 °C PBS, after which the solution was transferred to dialysis tubing (MWCO 12–14 kDa) and dialysed against deionised water at 40 °C for 7 d with water changes every 12 h. The dialysate was lyophilised for 48 h to yield GelMA.

GelMA (1.0 g) was redissolved in PBS (37 °C) to obtain 10 mL of a 10 % (w/v) pre-polymer solution, to which 100 μL of 100 mM 3-aminophenylboronic acid (3-APBA, in DMSO) and 500 μL of 10 mg mL^{-1} Irgacure 2959 were added sequentially. The mixture was processed in a microfluidic device at an aqueous-phase flow rate of 200 μL min^{-1} against an oil phase (HFE-7500 containing 2 % Krytox PEG-PFPE) at 800 μL min^{-1} to generate water-in-oil droplets, which were collected on ice. Droplets were photocross-linked under 365 nm UV irradiation (10 mW cm^{-2}) for 60 s, demulsified with 3 mL of perfluoro-1-octanol, washed three times with PBS, and sieved through a 100 μm mesh to obtain primary microspheres. The wet microspheres were suspended in 5 mL of 5 % (w/v) mannitol, flash-frozen in liquid nitrogen, and lyophilised for 24 h to generate a highly porous architecture. The dried particles were incubated overnight at 4 °C with gentle shaking in 10 mL of citric-acid-loaded PBS (100 mg mL^{-1}), centrifuged, and lyophilised again to afford ~100 mg of porous GelMA-APBA-citric-acid microspheres (GAC).

For liposome fabrication, 200 mg egg phosphatidylcholine, 50 mg cholesterol, and 20 mg DSPE-TK-PEG_{2000}-vicinal-diol were dissolved in 40 mL anhydrous ethanol containing 2 mg Mirdametinib, followed by ultrasonic dispersion. The mixture was subjected to rotary evaporation under reduced pressure at 50 °C for 30 min to form a thin film, which was further vacuum-dried for 2 h. The film was hydrated with 20 mL

of 55 °C PBS, extruded through a 220 nm polycarbonate membrane, and dialysed twice against PBS (MWCO 100 kDa) to remove free drug, yielding the liposomal formulation (LTM).

Finally, 50 mg of dried GAC microspheres were resuspended in 5 mL of 50 mM borate buffer (pH 8.5) and mixed with 5 mL of the LTM dispersion. The suspension was gently rotated at 4 °C for 2 h to allow boronate-diol condensation, producing the GelMA–liposome composite designated GAC@LTM.

Scanning electron microscopy (SEM) of GelMA-based microspheres

Lyophilised GelMA-APBA-citric-acid microspheres were dusted onto carbon-taped aluminium stubs and sputter-coated with a 5 nm layer of gold–palladium (Quorum Q150R ES; 8 mA, 45 s) under 5×10^{-2} mbar. Images were acquired on a field-emission SEM (Zeiss Sigma 500) operated at 5 kV accelerating voltage, 30 µm aperture and 6 mm working distance.

Negative-stain transmission electron microscopy (TEM) of liposomes

Liposomes were diluted to 0.1 mg mL^{-1} lipid in PBS and 10 µL of the suspension was placed on a glow-discharged 300-mesh copper grid coated with a continuous carbon film. After 1 min adsorption, excess liquid was wicked off with filter paper and the grid was immediately stained with 1 % (w/v) phosphotungstic acid, pH 7.0, for 60 s. The stain was blotted away, grids were air-dried for 15 min, and specimens were examined on a Tecnai G2 Spirit (FEI) operated at 120 kV.

Hydrodynamic diameter and zeta potential of liposomes

Dynamic light scattering (DLS) and electrophoretic light scattering were performed on a Zetasizer Nano ZS (Malvern Instruments) equipped with a 4 mW He–Ne laser (633 nm). Liposome dispersions were diluted 1:100 with filtered PBS to a lipid concentration of 0.2 mg mL^{-1} and equilibrated at 25 °C for 2 min in disposable polystyrene cuvettes (diameter measurements, back-scatter angle 173°). Zeta potential was recorded in folded capillary cells (DTS1070) at 25 °C; values were calculated with Smoluchowski's approximation.

TEM of microsphere–liposome composites

Composite particles were gently embedded in Spurr epoxy resin, and ultrathin sections (70 nm) were obtained on an ultramicrotome (Leica EM UC7) equipped with a diamond knife. Sections were collected on formvar-coated copper grids, post-stained with 2 % uranyl acetate for 8 min followed by Reynolds' lead citrate for 3 min, rinsed with CO_2-free water, and dried under vacuum. Imaging was performed on a JEM-2100F (JEOL) at 200 kV. The localisation of DSPE-TK-PEG liposomes on the microsphere surface, as well as the integrity of the internal porous network, were visualised in both bright-field and selected-area electron-diffraction modes.

FTIR, XPS and two-dimensional correlation infra-red (2D-IR) spectroscopy of microsphere–liposome composites

Freeze-dried GAC@LTM composites were milled to a fine powder, and ∼2 mg of each specimen was pressed against a diamond attenuated-total-reflection (ATR) crystal (Bruker Vertex 70). Spectra were collected from 4000 to 600 cm^{-1} (32 scans, 4 cm^{-1} resolution) and baseline-corrected in OPUS 7.5; differential spectra were obtained by subtracting spectra of native GelMA microspheres to highlight boronate-diol and thioketal signatures. X-ray photoelectron spectroscopy was carried out on a Kratos Axis Supra equipped with a monochromatic Al Kα source (1486.6 eV, 150 W). Survey scans (pass energy 160 eV) and high-resolution windows for C 1s, N 1s, O 1s, B 1s, P 2p and S 2p (pass energy 40 eV) were collected at 90° take-off; binding energies were charge-corrected to the C 1s peak at 284.8 eV. For 2D correlation IR, sequential ATR-FTIR spectra were recorded while the sample temperature was linearly ramped from 30 to 80 °C in 5 °C steps; synchronous and asynchronous maps were generated with 2DShige software to resolve overlapping bands associated with PEG-boronate dissociation and TK oxidation.

Degradation assay and drug release assay

For degradation and drug-release assays, freeze-dried GAC@LTM microspheres (10 mg, n = 3 per time point) were transferred into 2 mL polypropylene tubes containing 2

mL of release medium pre-equilibrated to 37 °C. Four media were employed: (i) pH 7.4 phosphate-buffered saline (PBS); (ii) pH 5.5 acetate-buffered saline; (iii) pH 7.4 PBS supplemented with 100 μM hydrogen peroxide; and (iv) pH 5.5 acetate buffer supplemented with 100 μM hydrogen peroxide. All buffers contained 0.1 mg mL^{-1} collagenase type II to simulate physiological enzymolysis, and H_2O_2-containing media were freshly spiked at each sampling to maintain the stated concentration. Samples were incubated horizontally at 37 °C on an orbital shaker (100 rpm). At predetermined intervals (0, 2, 4, 6, 8, 10day) tubes were centrifuged (300 g, 2 min, 25 °C). Pellets were rinsed twice with deionised water, lyophilised overnight and weighed to determine residual mass.

The tubes were centrifuged (300 g, 2 min, 25 °C) at predetermined time intervals (0, 2, 4, 8, 16, 24, 48, 72 h) using the method described above.Supernatants were collected for analytical quantification and replaced with equal volumes of fresh, pre-warmed buffer to preserve sink conditions. Citric acid released into the supernatants was quantified by reversed-phase HPLC equipped with a UV detector. Briefly, 20 μL samples were injected onto a C18 column (4.6 × 150 mm, 5 μm) eluted isocratically with 0.1 % (v/v) phosphoric acid in water at 0.6 mL min^{-1}, and detected at 210 nm; calibration curves (10–200 μg mL^{-1}) were prepared in the corresponding release medium. Mirdametinib concentrations were determined on the same instrument using a gradient method (mobile phase A, water + 0.1 % formic acid; mobile phase B, acetonitrile; 10 – 60 % B over 8 min; 0.4 mL min^{-1}; 262 nm). Prior to analysis, 200 μL of each sample was mixed 1:1 with ice-cold acetonitrile, vortexed, centrifuged (12 000 g, 10 min, 4 °C) and the clarified supernatant injected; external standards (0.5–50 μg mL^{-1}) were run in matching buffers. Supernatants from ROS groups were treated with catalase (100 U mL^{-1}, 5 min, 25 °C) before analysis to eliminate residual peroxide and protect the column.

Isolation, culture and treatment of rat NPCs

Primary NPCs were obtained from the coccygeal intervertebral discs of male Sprague–Dawley rats (8 weeks of age, 200-220 g). After euthanasia via carbon dioxide inhalation, NP tissues were carefully separated under sterile conditions and washed thoroughly

with phosphate-buffered saline (PBS) to remove residual blood and connective tissues. The isolated tissues were minced into small fragments and subjected to sequential enzymatic digestion using 0.25% trypsin for 30 min, followed by incubation with type II collagenase (10 mg/mL; Sigma–Aldrich, USA) at 37 °C for approximately 1-2 h under continuous agitation. Following digestion, the cell suspension was filtered and centrifuged at 400 ×g for 5 min to collect NPCs. The harvested cells were cultured in DMEM/F12 medium (Gibco, Grand Island, NY, USA) supplemented with 10% fetal bovine serum (Gibco) and 1% penicillin–streptomycin (Gibco). Cells were maintained in a humidified incubator containing 5% CO_2 at 37 °C, with the medium refreshed every 2–3 days. Cells at passages 2–3 were used for all subsequent in vitro experiments.

For adenovirus transfection, NPCs were incubated with OE-ETS2 (MOI = 100) or sh-ETS2 (MOI = 100) in medium without antibiotics. The infection medium was replaced by growth medium after 12 h. When performing sh-c-Jun transfection, in accordance with the recommendations of the product operation manual, the NPCs cultured to the third generation were placed in 6-well plates for culture. When the fusion was expanded to 70%, Lipo3000 was used for transfection at a rate of 100 nmol per well. In the drug intervention experiment, when rat NPCs in the culture dish were fused to 50%-60%, complete culture medium containing 50 ng/mL TNF-α or 0.5 μM MEKi or hydrogel microsphere was used for intervention.

RNA sequencing

Total RNA was isolated using TRIzol reagent according to the manufacturer's instructions. RNA integrity and quality were subsequently assessed using the Agilent 2100 Bioanalyzer (Agilent Technologies, CA, USA). Qualified RNA samples were further processed for library construction and high-throughput sequencing on the Illumina HiSeq platform. Differential gene expression analysis was conducted using the DESeq2 package (version 1.20.0) in R software. Genes with a P value < 0.05 were defined as significantly differentially expressed. Functional enrichment analyses, including Gene Ontology (GO) annotation and Kyoto Encyclopedia of Genes and Genomes (KEGG) pathway analysis, were performed using the clusterProfiler package in R package.

Western blot analysis

Total proteins from NP tissues and cultured cells were extracted using RIPA lysis buffer (Beyotime, Shanghai, China) supplemented according to the manufacturer's protocol. Protein concentrations were quantified using a bicinchoninic acid (BCA) protein assay kit (Beyotime, Shanghai, China). Equal amounts of protein samples (20 μg per lane) were separated by sodium dodecyl sulfate–polyacrylamide gel electrophoresis (SDS–PAGE) and subsequently transferred onto polyvinylidene fluoride (PVDF) membranes (Millipore, MA, USA).

After transfer, membranes were blocked with 5% bovine serum albumin (BSA, BioFroxx, Germany) at room temperature for 1 h, followed by incubation with the indicated primary antibodies including ETS2 (1:1000, ab219948, Abcam), ACAN (1:1000, DF7561, Affinity), Collagen II (1:1000, AF0135, Affinity), MMP13 (1:1000, AF5355, Affinity), TNFR (1:1000, 13377T, CST), p21 (1:1000, ab109199, Abcam), p16 (1:1000, ab51243, Abcam) and c-Jun (1:1000, ab40766, Abcam) overnight at 4 °C. On the following day, membranes were incubated with corresponding horseradish peroxidase-conjugated secondary antibodies (1:1000, SA00001-2, Proteintech) for 1 h at room temperature. After three washes with TBST, immunolabeling was activated by an Omni-ECL™ Femto Light Chemiluminescence Kit (SQ201, Epizyme, Shanghai, China) and captured by a GeneGnome XRQ analyzer (Syngen, Cambridge, UK). Gray value was analyzed using ImageJ normalized to GAPDH.

Co-Immunoprecipitation (Co-IP)

NPCs were lysed in IP lysis buffer and clarified by centrifugation at 12,000 rpm for 15 min at 4 °C. The resulting supernatants were incubated overnight at 4 °C with 1 μL primary antibodies including ETS2 (1:1000, ab219948, Abcam) or c-Jun (1:1000, ab40766, Abcam) in the presence of Protein A magnetic beads (MedChemExpress). Following extensive washing to remove nonspecific interactions, the immunoprecipitated complexes were eluted in loading buffer and analyzed by western blotting using the indicated antibodies.

Dual-luciferase assay

HEK 293T cells were seeded into 12-well plates (1 × 105) and transfected with the c-Jun-promoter-luciferase plasmid (Vigene Biosciences) and the renilla reniformis luciferase plasmid (Vigene Biosciences). Then, transfected NPCs were treated with Ad-ETS2 for 24 h. The Dual-Luciferase Reporter Assay System kit (Promega, WI, USA) was used to activate the activities of luciferase, which were detected by a microplate reader (BioTek, VT, USA).

Biocompatibility evaluations

In the in vitro biocompatibility assessment, sterilized hydrogel microspheres were co-cultured with NPCs, and cell viability was detected by live/dead cell staining and CCK-8. In the in vivo biocompatibility assessment, needle puncture model in SD rats was established. Hydrogel microspheres were implanted into animal NP tissue for 2 weeks. Subsequently, all the experimental animals were euthanized. Fresh whole blood was collected for hemolysis experiments and a series of biochemical tests, and heart, liver, spleen, lung and kidney tissues were extracted for HE staining.

Immunofluorescence (IF) assay

For immunofluorescence analysis, NPCs were cultured and treated according to the experimental protocols described above. Cells were fixed with 4% paraformaldehyde, permeabilized with 0.2% Triton X-100, and blocked in 1% BSA before incubation with primary antibodies against ETS2 (1:1000, ab219948, Abcam), c-Jun (1:1000, ab280089, Abcam), ACAN (1:1000, DF7561, Affinity), Collagen II (1:1000, AF0135, Affinity), MMP13 (1:1000, AF5355, Affinity) and p21 (1:1000, ab109199, Abcam) overnight at 4 °C. After washing, samples were incubated with the corresponding fluorescent secondary antibodies and counterstained with DAPI. Fluorescence images were acquired using an EVOS FL Auto Imaging System (Thermo Fisher Scientific).

β-galactosidase staining and ROS level detection

After co-culturing NPCs with hydrogel microspheres, wash with phosphate buffer, add an appropriate amount of fixative and fix at room temperature for 15 min. After washing

again, add freshly prepared SA-β-gal staining working solution (Beyotime, Shanghai, China) and incubate overnight in the dark at 37 °C without carbon dioxide. After the reaction was terminated, the blue-green positive staining signal was observed under an optical microscope. Intracellular ROS levels were evaluated by staining with dichloro-dihydro-fluorescein diacetate working solution (Beyotime, Shanghai, China) for 20 min, followed by fluorescence microscopy for observation.

Experimental design of needle puncture model and treatment

To establish the IDD model and evaluate intervention effect, male SD rats (8 weeks of age, 200-220 g) were included in this study. Prior to surgery, all animals were anesthetized via intraperitoneal injection of 2% pentobarbital sodium (30 mg/kg). Firstly, Ad-ETS2 was used to up-regulate ETS2 expression levels in NP tissues. Six rat tail intervertebral disc were subjected to the same treatment: Co6/7 disc was exposed and followed by suture as SHAM treatment; Co7/8 and Co8/9 disc were injected with Ad-NC and Ad-ETS2 by a 31-gauge Hamilton syringe (Hamilton, NV, USA), respectively. Secondly, Ad-sh-ETS2 or MEKi was used to inhibit ETS2 in degenerative NP tissues. Twelve rats were randomly divided into two groups: Co6/7 disc was exposed and followed by suture as SHAM treatment; Co7/8 disc NP tissue was punctured by a 21-gauge outer diameter needle for 10 s and rotated twice; Co8/9 disc NP tissue received Ad-sh-ETS2 or MEKi (0.5 μM) injection after disc puncture. Lastly, Seven rats were randomly divided into seven groups: intervertebral discs of Co6/7 to Co10/11 in each group were injected with G, GA, GC, GAC, GAC@L, GAC@LT, GAC@LTM respectively after disc puncture. At 4 weeks after surgery, imaging analysis and histological staining were performed on the rat's intervertebral disc tissues in both experiments.

Magnetic resonance imaging (MRI)

For MRI assessment, rats were anesthetized using 2% isoflurane delivered in oxygen and positioned prone on the examination platform with the tail maintained in a straight alignment. MRI examinations were conducted using a 3.0-T clinical scanner (Siemens, Shanghai, China). T2-weighted coronal sequences of the intervertebral discs were

acquired consecutively with a dedicated dual-tuned volume radiofrequency coil. A total of 9-11 continuous image sections were collected for each specimen. The degree of disc degeneration was subsequently evaluated based on MRI findings using the modified Pfirrmann grading system.

Micro-CT and X-ray

Following euthanasia, rat tail intervertebral disc specimens were harvested and subjected to micro-computed tomography (micro-CT) analysis. Imaging was conducted using a micro-CT 50 system (Scanco Medical, Zurich, Switzerland). Scanning parameters were configured at a voxel resolution of 18 μm, with an operating voltage of 100 kV and a current of 98 μA. Three-dimensional reconstructed CT images and corresponding radiographic images were generated using the manufacturer-provided evaluation software integrated within the micro-CT system. Quantitative assessment of disc degeneration was subsequently performed by calculating the disc height index (DHI) from X-ray images, according to previously established methods.[89]

Histological staining and immunohistochemistry (IHC)

Harvested coccygeal intervertebral disc tissues were fixed in 4% paraformaldehyde, paraffin-embedded, and sectioned at 4 μm thickness. Tissue morphology was assessed by HE and Safranin O/Fast Green staining following standard protocols. For immunohistochemistry, sections were incubated with the indicated primary antibodies including ETS2 (1:1000, ab219948, Abcam), Collagen II (1:1000, AF0135, Affinity) and MMP13 (1:1000, AF5355, Affinity) followed by HRP-conjugated secondary antibodies and DAB development. Images were captured using an EVOS FL Auto Imaging System (Thermo Fisher Scientific). Histological changes associated with disc degeneration were quantified using a previously established histological grading system.

Statistical analysis

Statistical analyses were carried out using GraphPad Prism 10.0 (GraphPad Software, USA). Data are expressed as mean ± SD unless otherwise indicated. Differences among

groups were assessed by one-way ANOVA, whereas ordinal variables such as histological and Pfirrmann scores were evaluated using the Kruskal–Wallis test. Statistical significance was defined as $P < 0.05$.

Acknowledgements

This work was supported by the National Nature Science Foundation of China (No. 82002345 to J.D., No. 82572432 to Y.Q.), the Health Commission Medical Research General Program of Jiangsu Province (M2024107 to J.D.).

Author contributions

J.D., Y.Q. and B.L. conceived the study, directed, and supervised the research. J.N. performed most experiments, collected all the data, participated in the analysis of results, presented the data in publishable figures, and wrote the paper. H.S. contributed to preparation and characterization of hydrogel microspheres. K.W. contributed to experimental protocol design. X.Zhang., Y.W., Y.C., H.L., M.J., Z.Z., L.S. and X.Zhou. participated in project discussions and data analysis. All authors have read and approved the article.

Competing interests

The authors declare that they have no competing interests.

Contributor Information

Jun Dai, Email: daijun@suda.edu.cn.

Yusen Qiao, Email: qiaoyusen8612@suda.edu.cn.

Bin Li, Email: binli@suda.edu.cn.

References

1. Fine, N. *et al.* Intervertebral disc degeneration and osteoarthritis: a common molecular disease spectrum. *Nat Rev Rheumatol* **19**, 136–152 (2023).
2. Vos, T. *et al.* Years lived with disability (YLDs) for 1160 sequelae of 289 diseases and injuries 1990-2010: a systematic analysis for the Global Burden of Disease Study 2010. *Lancet* **380**,

2163–2196 (2012).

3. Kibble, M. J. *et al.* Suspension bioprinted whole intervertebral disc analogues enable regional stiffness- and hypoxia-regulated matrix secretion by primary human nucleus pulposus and annulus fibrosus cells. *Acta Biomater* S1742-7061(25)00340-X (2025) doi:10.1016/j.actbio.2025.05.015.
4. Eisenstein, S. M., Balain, B. & Roberts, S. Current Treatment Options for Intervertebral Disc Pathologies. *Cartilage* **11**, 143–151 (2020).
5. Kang, L., Zhang, H., Jia, C., Zhang, R. & Shen, C. Epigenetic modifications of inflammation in intervertebral disc degeneration. *Ageing Research Reviews* **87**, 101902 (2023).
6. Risbud, M. V. & Shapiro, I. M. Role of cytokines in intervertebral disc degeneration: pain and disc content. *Nat Rev Rheumatol* **10**, 44–56 (2014).
7. Dou, Y. *et al.* Role of macrophage in intervertebral disc degeneration. *Bone Res* **13**, 15 (2025).
8. Huang, Y.-C., Urban, J. P. G. & Luk, K. D. K. Intervertebral disc regeneration: do nutrients lead the way? *Nat Rev Rheumatol* **10**, 561–566 (2014).
9. Luo, Y. *et al.* Cooperative Binding of ETS2 and NFAT Links Erk1/2 and Calcineurin Signaling in the Pathogenesis of Cardiac Hypertrophy. *Circulation* **144**, 34–51 (2021).
10. Stankey, C. T. *et al.* A disease-associated gene desert directs macrophage inflammation through ETS2. *Nature* **630**, 447–456 (2024).
11. Wang, X. *et al.* Pharmacological network analysis of the functions and mechanism of kaempferol from Du Zhong in intervertebral disc degeneration (IDD). *J Orthop Translat* **39**, 135–146 (2023).
12. Qin, D. *et al.* Supercharging CAR-T cells through transcriptional and epigenetic armoring. *Theranostics* **15**, 3345–3367 (2025).
13. Sanlorenzo, M. *et al.* Systemic IFN-I combined with topical TLR7/8 agonists promotes distant tumor suppression by c-Jun-dependent IL-12 expression in dendritic cells. *Nat Cancer* **6**, 175–193 (2025).
14. Zhang, R. *et al.* c-JUN: a chromatin repressor that limits mesoderm differentiation in human pluripotent stem cells. *Nucleic Acids Res* **53**, gkaf001 (2025).
15. Cobo, I. *et al.* Particle uptake by macrophages triggers bifurcated transcriptional pathways that differentially regulate inflammation and lysosomal gene expression. *Immunity* **58**, 826-842.e8 (2025).

16. Li, L., Zhang, G., Yang, Z. & Kang, X. Stress-Activated Protein Kinases in Intervertebral Disc Degeneration: Unraveling the Impact of JNK and p38 MAPK. *Biomolecules* **14**, 393 (2024).
17. Xu, W. *et al.* PDE4B promotes JNK/NLRP3 activation in the nucleus pulposus and mediates intervertebral disc degeneration. *Sci Rep* **15**, 5739 (2025).
18. Basuyaux, J. P., Ferreira, E., Stéhelin, D. & Butticè, G. The Ets Transcription Factors Interact with Each Other and with the c-Fos/c-Jun Complex via Distinct Protein Domains in a DNA-dependent and -independent Manner. *Journal of Biological Chemistry* **272**, 26188–26195 (1997).
19. Zhao, X. *et al.* Photocrosslinkable Gelatin Hydrogel for Epidermal Tissue Engineering. *Adv Healthc Mater* **5**, 108–118 (2016).
20. Das, S. *et al.* Bioprintable, cell-laden silk fibroin-gelatin hydrogel supporting multilineage differentiation of stem cells for fabrication of three-dimensional tissue constructs. *Acta Biomater* **11**, 233–246 (2015).
21. Maurer, P. H. II. Antigenicity of gelatin in rabbits and other species. *J Exp Med* **100**, 515–523 (1954).
22. B, L. *et al.* Recent advances in GelMA hydrogel transplantation for musculoskeletal disorders and related disease treatment. *Theranostics* **13**, (2023).
23. Kurian, A. G., Singh, R. K., Patel, K. D., Lee, J.-H. & Kim, H.-W. Multifunctional GelMA platforms with nanomaterials for advanced tissue therapeutics. *Bioact Mater* **8**, 267–295 (2022).
24. Wang, W. An anti-senescence hydrogel with pH-responsive drug release for mitigating intervertebral disc degeneration and low back pain. *Bioactive Materials* (2024).
25. Chen, X. *et al.* The role of oxidative stress in intervertebral disc degeneration: Mechanisms and therapeutic implications. *Ageing Res Rev* **98**, 102323 (2024).
26. Ma, L. *et al.* Enhanced Mechanical Properties and Sensing Performance of MXene-Based Dual-Crosslinked Hydrogel via EGCG Coating and Dynamic Covalent Bond. *Small* **21**, e2501322 (2025).
27. Zhou, J. *et al.* Large-scale RNAi screen identified Dhpr as a regulator of mitochondrial morphology and tissue homeostasis. *Sci Adv* **5**, eaax0365 (2019).
28. Kang, L. *et al.* The mitochondria-targeted anti-oxidant MitoQ protects against intervertebral disc degeneration by ameliorating mitochondrial dysfunction and redox imbalance. *Cell Prolif* **53**, e12779 (2020).

29. Tschoeke, S. K. *et al.* Apoptosis of human intervertebral discs after trauma compares to degenerated discs involving both receptor-mediated and mitochondrial-dependent pathways. *J Orthop Res* **26**, 999–1006 (2008).
30. Zhou, R., Yazdi, A. S., Menu, P. & Tschopp, J. A role for mitochondria in NLRP3 inflammasome activation. *Nature* **469**, 221–225 (2011).
31. Xue, C. *et al.* Reactive oxygen species (ROS)-mediated M1 macrophage-dependent nanomedicine remodels inflammatory microenvironment for osteoarthritis recession. *Bioact Mater* **33**, 545–561 (2024).
32. Indurkar, A., Rubenis, K., Boccaccini, A. R. & Locs, J. Development of nanocomposite hydrogel using citrate-containing amorphous calcium phosphate and gelatin methacrylate. *Front Bioeng Biotechnol* **12**, 1421415 (2024).
33. He, R. *et al.* HIF1A Alleviates compression-induced apoptosis of nucleus pulposus derived stem cells via upregulating autophagy. *Autophagy* **17**, 3338–3360 (2021).
34. Song, C. *et al.* Integrated metagenomic and metabonomic mechanisms for the therapeutic effects of Duhuo Jisheng decoction on intervertebral disc degeneration. *PLoS One* **19**, e0310014 (2024).
35. Sawamura, M., Arai, T. & Kawasumi, K. Effect of acupuncture on the energy metabolism of dogs with intervertebral disk disease and cervical disk herniation: A pilot study. *Vet Res Commun* **47**, 879–884 (2023).
36. Qian, B. *et al.* The involvement of SigmaR1K142 degradation mediated by ERAD in neural senescence linked with CdCl2 exposure. *J Hazard Mater* **472**, 134466 (2024).
37. Long, Z. & Qin, Q. Impact of Socioeconomic Status on the Risk of Intervertebral Disc Degeneration and Low Back Pain in the European Population and the Mediating Role of Obesity-Related Traits: Evidence from a Mendelian Randomization Study. *J Pain Res* **18**, 1627–1641 (2025).
38. Hammoor, B. T. *et al.* Intervertebral disc degeneration. *Nat Rev Dis Primers* **12**, 5 (2026).
39. Shi, L. *et al.* Cell-based therapies for intervertebral disc degeneration: Navigating the path from promise to clinical reality. *J Orthop Translat* **56**, 101041 (2026).
40. Sakai, D. & Andersson, G. B. J. Stem cell therapy for intervertebral disc regeneration: obstacles and solutions. *Nat Rev Rheumatol* **11**, 243–256 (2015).
41. Yang, L. *et al.* EGF suppresses the expression of miR-124a in pancreatic β cell lines via ETS2

activation through the MEK and PI3K signaling pathways. *Int J Biol Sci* **15**, 2561–2575 (2019).

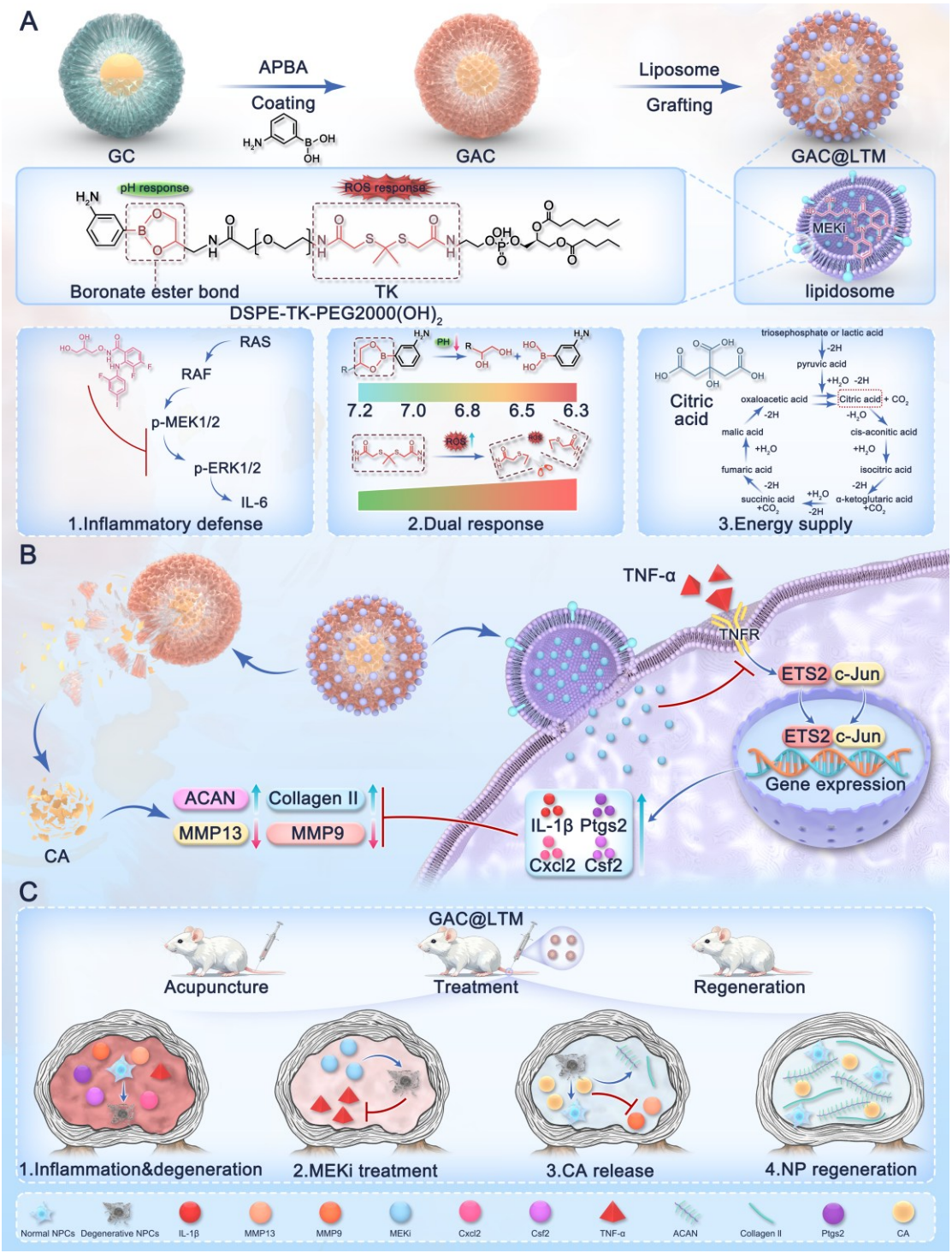
42. Singh, A. K. *et al.* Ets-2 Propagates IL-6 Trans-Signaling Mediated Osteoclast-Like Changes in Human Rheumatoid Arthritis Synovial Fibroblast. *Front Immunol* **12**, 746503 (2021).
43. Xu, Q., Ma, P., Wang, R., Feng, G. & Jin, Q. Prediction and validation based on scRNA-seq: ETS2 targets CEBPB to mediate osteoclast differentiation in osteoarthritis progression. *Int J Biol Macromol* **319**, 145639 (2025).
44. Tao, C. *et al.* Inactivation of Tnf-α/Tnfr signaling attenuates progression of intervertebral disc degeneration in mice. *JOR Spine* **7**, e70006 (2024).
45. Yi, W. *et al.* Impact of NF-κB pathway on the apoptosis-inflammation-autophagy crosstalk in human degenerative nucleus pulposus cells. *Aging (Albany NY)* **11**, 7294–7306 (2019).
46. Li, L., Zhang, G., Yang, Z. & Kang, X. Stress-Activated Protein Kinases in Intervertebral Disc Degeneration: Unraveling the Impact of JNK and p38 MAPK. *Biomolecules* **14**, 393 (2024).
47. Fan, C. *et al.* M1 macrophage-derived exosomes promote intervertebral disc degeneration by enhancing nucleus pulposus cell senescence through LCN2/NF-κB signaling axis. *J Nanobiotechnology* **22**, 301 (2024).
48. Hu, B. *et al.* Heme oxygenase-1 attenuates IL-1β induced alteration of anabolic and catabolic activities in intervertebral disc degeneration. *Sci Rep* **6**, 21190 (2016).
49. Mern, D. S. & Thomé, C. Collagen II enrichment through scAAV6-RNAi-mediated inhibition of matrix-metalloproteinases 3 and 13 in degenerative nucleus-pulposus cells degenerative disc disease and biological treatment strategies. *Exp Biol Med (Maywood)* **249**, 10048 (2024).
50. Yao, Z. *et al.* Salubrinal Suppresses IL-17-Induced Upregulation of MMP-13 and Extracellular Matrix Degradation Through the NF-kB Pathway in Human Nucleus Pulposus Cells. *Inflammation* **39**, 1997–2007 (2016).
51. Cai, F. *et al.* The Paracrine Effect of Degenerated Disc Cells on Healthy Human Nucleus Pulposus Cells Is Mediated by MAPK and NF-κB Pathways and Can Be Reduced by TGF-β1. *DNA Cell Biol* **36**, 143–158 (2017).
52. Jacobsen, T. D. *et al.* TNFα Receptor 1 and Not Receptor 2 Affect Annulus Fibrosus and Nucleus Pulposus Response to Cytokine Challenge in a Rat Model. *JOR Spine* **8**, e70070 (2025).
53. Chen, L. *et al.* Nuclear factor-kappa B-dependent X-box binding protein 1 signalling promotes the proliferation of nucleus pulposus cells under tumour necrosis factor alpha stimulation. *Cell Prolif* **52**, e12542 (2019).

54. Tao, C. *et al.* Inactivation of Tnf-α/Tnfr signaling attenuates progression of intervertebral disc degeneration in mice. *JOR Spine* **7**, e70006 (2024).
55. Zhou, N. *et al.* SIRT1 alleviates senescence of degenerative human intervertebral disc cartilage endo-plate cells via the p53/p21 pathway. *Sci Rep* **6**, 22628 (2016).
56. Ding, J. *et al.* ASIC1 and ASIC3 mediate cellular senescence of human nucleus pulposus mesenchymal stem cells during intervertebral disc degeneration. *Aging (Albany NY)* **13**, 10703–10723 (2021).
57. Chen, J. *et al.* Sirt6 overexpression suppresses senescence and apoptosis of nucleus pulposus cells by inducing autophagy in a model of intervertebral disc degeneration. *Cell Death Dis* **9**, 56 (2018).
58. Gu, T. *et al.* CircFUNDC1 interacts with CDK9 to promote mitophagy in nucleus pulposus cells under oxidative stress and ameliorates intervertebral disc degeneration. *Cell Death Dis* **16**, 94 (2025).
59. Feng, C. *et al.* Oxygen-Sensing Nox4 Generates Genotoxic ROS to Induce Premature Senescence of Nucleus Pulposus Cells through MAPK and NF-κB Pathways. *Oxid Med Cell Longev* **2017**, 7426458 (2017).
60. Yang, M. *et al.* Sirtuin 2 expression suppresses oxidative stress and senescence of nucleus pulposus cells through inhibition of the p53/p21 pathway. *Biochem Biophys Res Commun* **513**, 616–622 (2019).
61. Shi, Y. *et al.* Rescuing Nucleus Pulposus Cells From Senescence via Dual-Functional Greigite Nanozyme to Alleviate Intervertebral Disc Degeneration. *Adv Sci (Weinh)* **10**, e2300988 (2023).
62. Li, P., Zhang, M., Chen, Z., Tian, B. & Kang, X. Tissue-Engineered Injectable Gelatin-Methacryloyl Hydrogel-Based Adjunctive Therapy for Intervertebral Disc Degeneration. *ACS Omega* **8**, 13509–13518 (2023).
63. Lv, B. *et al.* Recent advances in GelMA hydrogel transplantation for musculoskeletal disorders and related disease treatment. *Theranostics* **13**, 2015–2039 (2023).
64. Tian, X. *et al.* Bioinspired hydrogel microspheres enhance nucleus pulposus regeneration through N-cadherin interaction with extracellular matrix mimicry. *J Control Release* **383**, 113771 (2025).
65. Wang, F. *et al.* Kartogenin-loaded hydrogel promotes intervertebral disc repair via protecting MSCs against reactive oxygen species microenvironment by Nrf2/TXNIP/NLRP3 axis. *Free*

Radic Biol Med **204**, 128–150 (2023).

66. Heltmann-Meyer, S. *et al.* Gelatin methacryloyl is a slow degrading material allowing vascularization and long-term usein vivo. *Biomed Mater* **16**, (2021).
67. Yang, S. *et al.* Harnessing Anti-Inflammatory and Regenerative Potential: GelMA Hydrogel Loaded with IL-10 and Kartogenin for Intervertebral Disc Degeneration Therapy. *ACS Biomater Sci Eng* **11**, 1486–1497 (2025).
68. Dai, J. *et al.* Esterase-responsive kartogenin composite hydrogel microspheres boost nucleus pulposus regeneration in intervertebral disc degeneration. *Acta Biomater* **198**, 131–150 (2025).
69. Ben Messaoud, G., Aveic, S., Wachendoerfer, M., Fischer, H. & Richtering, W. 3D Printable Gelatin Methacryloyl (GelMA)-Dextran Aqueous Two-Phase System with Tunable Pores Structure and Size Enables Physiological Behavior of Embedded Cells In Vitro. *Small* **19**, e2208089 (2023).
70. Hong, Y. *et al.* IL-1ra loaded chondroitin sulfate-functionalized microspheres for minimally invasive treatment of intervertebral disc degeneration. *Acta Biomater* **185**, 336–349 (2024).
71. Wang, H. *et al.* GelMA hydrogels guide lineage-specific self-assembly of endothelial and interstitial cells into valve-mimetic tissue architectures. *Int J Biol Macromol* **339**, 149902 (2026).
72. Chou, H.-D. *et al.* Synthesis, Properties, and Biocompatibility of 4-Carboxyphenyboronic Acid-Modified Gelatin-Methacryloyl: A Hydrogel for Retinal Surgeries. *ACS Omega* **9**, 42147–42158 (2024).
73. Furikado, Y. *et al.* Universal reaction mechanism of boronic acids with diols in aqueous solution: kinetics and the basic concept of a conditional formation constant. *Chemistry* **20**, 13194–13202 (2014).
74. Cao, J. *et al.* An engineering-reinforced extracellular vesicle-integrated hydrogel with an ROS-responsive release pattern mitigates spinal cord injury. *Sci Adv* **11**, eads3398 (2025).
75. Nair, R. R. *et al.* Advances in phenylboronic acid and phenylboronic ester-based responsive systems for precision medicine. *Biomater Sci* **14**, 661–683 (2026).
76. Ding, J.-Y. *et al.* Anti-Senescent Biomaterials for Breaking Intervertebral Disc Degeneration. *Engineering* **53**, 259–285 (2025).
77. Snuggs, J. *et al.* Understanding the Physiological Behavior of Disc Cells in an In Vitro Imitation of the Healthy and Degenerated Disc Niche. *JOR Spine* **8**, e70153 (2025).

78. Zhou, H. *et al.* Role of oxidative stress in mitochondrial dysfunction and their implications in intervertebral disc degeneration: Mechanisms and therapeutic strategies. *J Orthop Translat* **49**, 181–206 (2024).
79. Gennari, A. *et al.* Revisiting Boronate/Diol Complexation as a Double Stimulus-Responsive Bioconjugation. *Bioconjug Chem* **28**, 1391–1402 (2017).
80. Feng, X., Zhang, Y., Chen, S. & Ding, Y. Acid-responsive metal organic frameworks with photothermal effects for osteoarthritis multiple therapy. *RSC Adv* **16**, 7271–7286 (2026).
81. Zhao, C. *et al.* Structural Transformative Antioxidants for Dual-Responsive Anti-Inflammatory Delivery and Photoacoustic Inflammation Imaging. *Angew Chem Int Ed Engl* **60**, 14458–14466 (2021).
82. Sun, W. *et al.* Environmental adaptive nanoplatform for bacteriotherapy. *Chemical Engineering Journal* **524**, 169148 (2025).
83. Li, Z. *et al.* A reactive oxygen species-responsive hydrogel encapsulated with bone marrow derived stem cells promotes repair and regeneration of spinal cord injury. *Bioact Mater* **19**, 550–568 (2023).
84. Liu, B. & Thayumanavan, S. Mechanistic Investigation on Oxidative Degradation of ROS-Responsive Thioacetal/Thioketal Moieties and Their Implications. *Cell Reports Physical Science* **1**, 100271 (2020).
85. Zhang, J. *et al.* ROS-degradable hydrogel delivering LOXL2-LNPs rescues disc degeneration by synchronously suppressing cellular senescence and oxidative damage. *J Nanobiotechnology* **23**, 652 (2025).
86. Bahar, M. E., Kim, H. J. & Kim, D. R. Targeting the RAS/RAF/MAPK pathway for cancer therapy: from mechanism to clinical studies. *Signal Transduct Target Ther* **8**, 455 (2023).
87. Sarin, K. Y. *et al.* Development of a MEK inhibitor, NFX-179, as a chemoprevention agent for squamous cell carcinoma. *Sci Transl Med* **15**, eade1844 (2023).
88. Sarin, K. Y. *et al.* Effect of NFX-179 MEK inhibitor on cutaneous neurofibromas in persons with neurofibromatosis type 1. *Sci Adv* **10**, eadk4946 (2024).
89. Lu, R. *et al.* Physalin A alleviates intervertebral disc degeneration via anti-inflammatory and anti-fibrotic effects. *J Orthop Translat* **39**, 74–87 (2023).



Scheme. 1. Schematic illustration of pH/ROS dual-responsive methacrylate gelatin (GelMA) microspheres for NP tissue regeneration. **A** Preparation protocols of dual-responsive microspheres, including CA embedding, APBA coating, liposome grafting and MEKi drug embedding. **B** GAC@LTM microspheres local delivery CA and MEKi, by ETS2/c-Jun signal axis to reduce inflammation, promote ECM regeneration. **C** A diagram showing IDD delay and NP regeneration mechanism: In the early stage of the IDD process, NP tissues are in an inflammatory

microenvironment. GAC@LTM microspheres release MEKi to inhibit inflammatory responses and CA to counteract oxidative stress, jointly promoting transformation of degenerative NPCs to normal NPCs and regeneration of NP tissues.

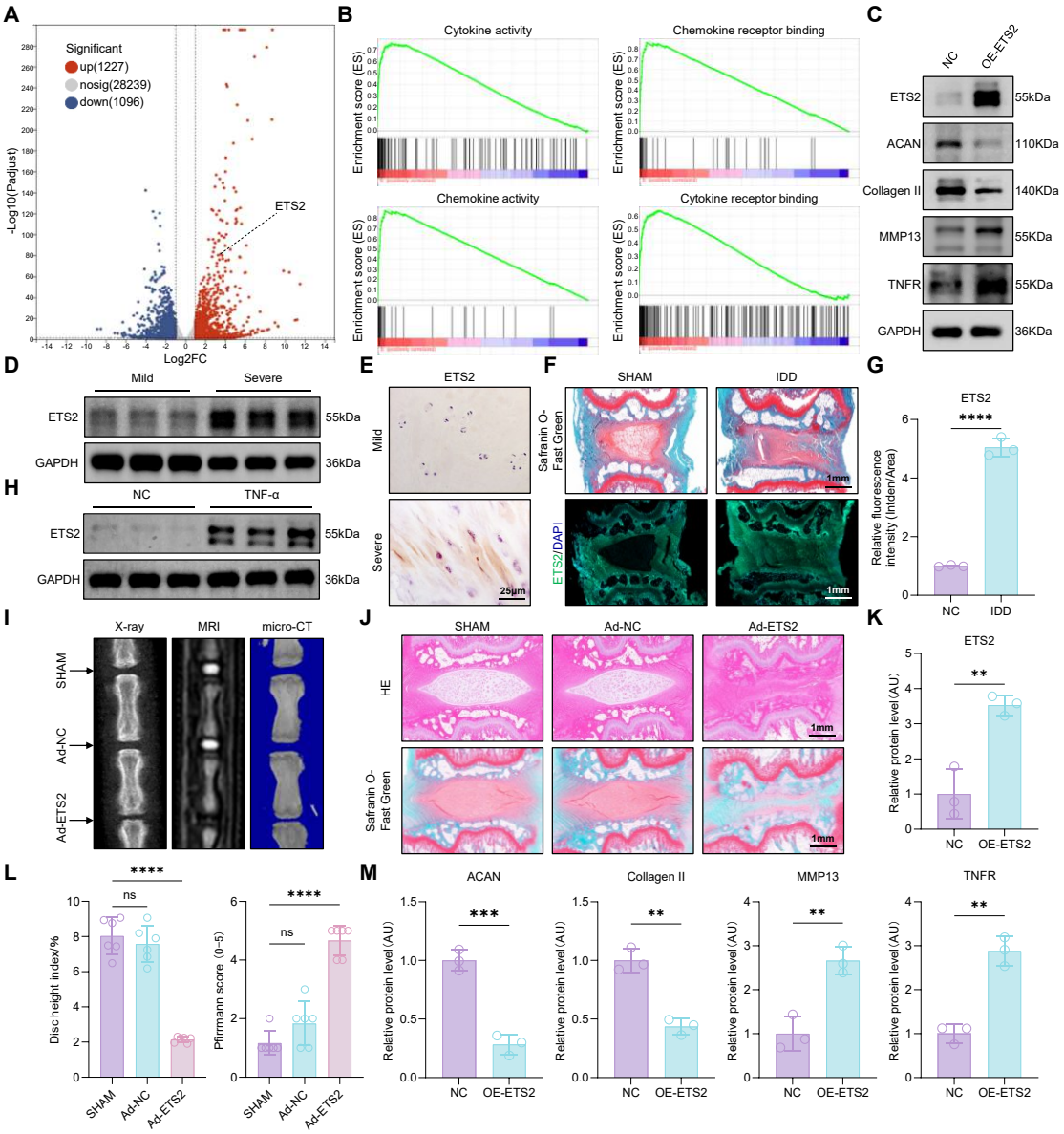


Fig. 1. ETS2 is highly expressed in degenerated NP tissue. **A** A volcano plot visually represents differential expression profiling of 1227 upregulated and 1069 downregulated genes, as determined by comprehensive RNA-sequencing analysis. **B** GSEA reveals significant activation of pathways related to cytokines and chemokines. **C** Western blot of ETS2, ACAN, Collagen II, MMP13, TNFR expression in NPCs transfected with OE-ETS2 for 24 h (n = 3). **D** Western blot of ETS2 expression in clinical NP samples (n = 3). **E** Immunohistochemistry of ETS2 expression in clinical NP samples. Scale bar = 25 μm. **F**, **G** Safranin O/fast green staining and immunofluorescence and quantification of ETS2 expression in rat intervertebral discs at 4 weeks after puncture. Scale bar = 1000 μm. **H** Western blot of ETS2 expression in NPCs treated with TNF-α for 24 h (n = 3). **I** X-ray, MRI and micro-CT images of rat intervertebral discs. **J** Histological staining images of intervertebral discs at 4 weeks after treatment. Scale bar = 1000 μm. **K** Quantification of western blot of ETS2 expression

in NPCs transfected with OE-ETS2 for 24 h (n = 3). **L** Disc height index quantification and Pfirrmann score quantification. **M** Quantification of western blot of ACAN, Collagen II, MMP13, TNFR expression in NPCs transfected with OE-ETS2 for 24 h (n = 3). Mean ± SEM, ns non-significant, $^{**}P < 0.01$, $^{***}P < 0.001$, $^{****}P < 0.0001$.

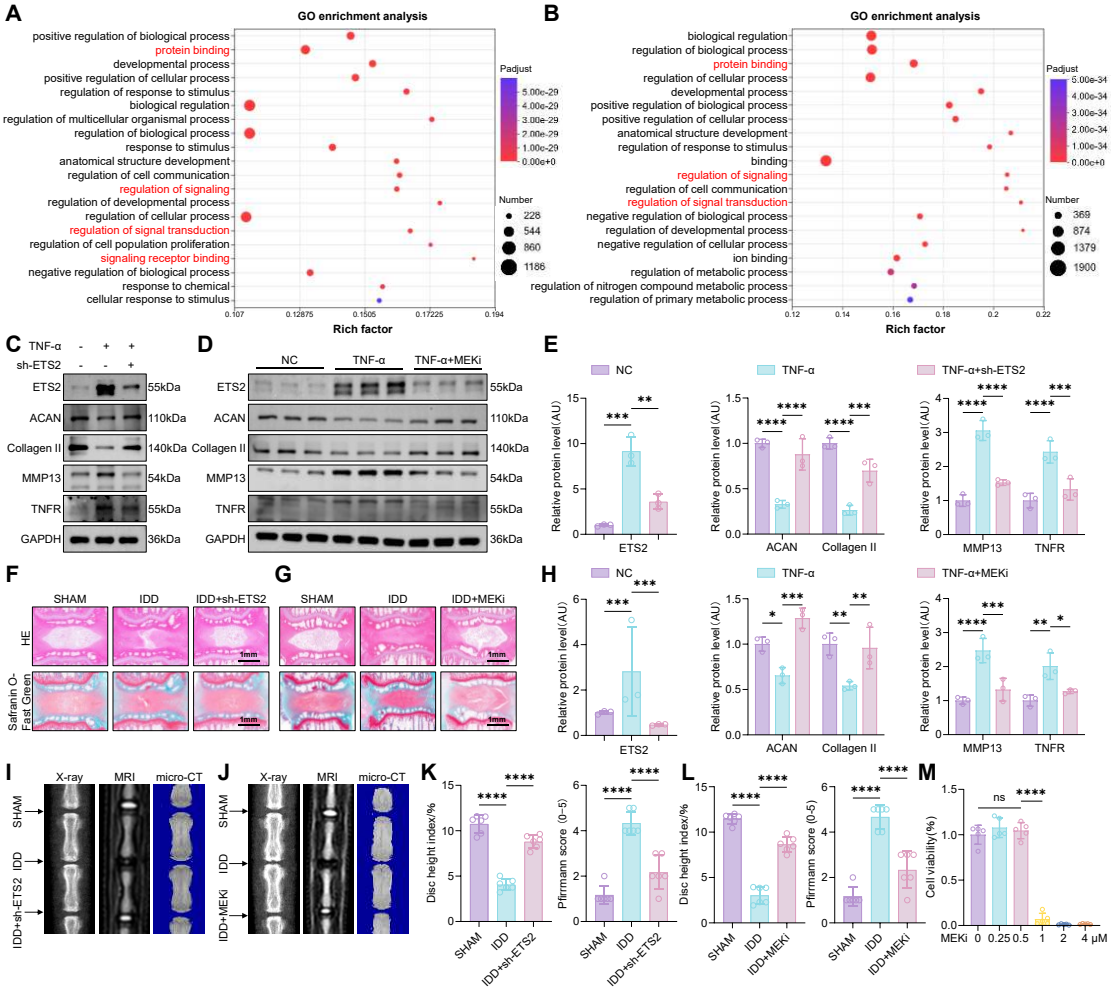


Fig. 2. Inhibition of ETS2 reduces inflammatory response of NPCs and delays IDD progression. **A**, **B** GO enrichment scatter plot of RNA-seq. **C** Western blot of ETS2, ACAN, Collagen II, MMP13, TNFR expression in NPCs transfected with sh-ETS2 and treated with TNF-α for 24 h (n = 3). **D** Western blot of ETS2, ACAN, Collagen II, MMP13, TNFR expression in NPCs treated with TNF-α and MEKi for 24 h (n = 3). **E** Quantification of western blot of ETS2, ACAN, Collagen II, MMP13, TNFR expression in NPCs transfected with sh-ETS2 and treated with TNF-α for 24 h (n = 3). **F**, **G** Histological staining images of intervertebral discs at 4 weeks after treatment. Scale bar = 1000 μm. **H** Quantification of western blot of ETS2, ACAN, Collagen II, MMP13, TNFR expression in NPCs treated with TNF-α and MEKi for 24 h (n = 3). **I**, **J** X-ray, MRI and micro-CT images of rat intervertebral discs. **K**, **L** Disc height index quantification and Pfirrmann score quantification. **M** Cell viability of NPCs treated with different concentrations of MEKi for 24 h. Mean ± SEM, $*P < 0.05$, $**P < 0.01$, $***P < 0.001$, $****P < 0.0001$.

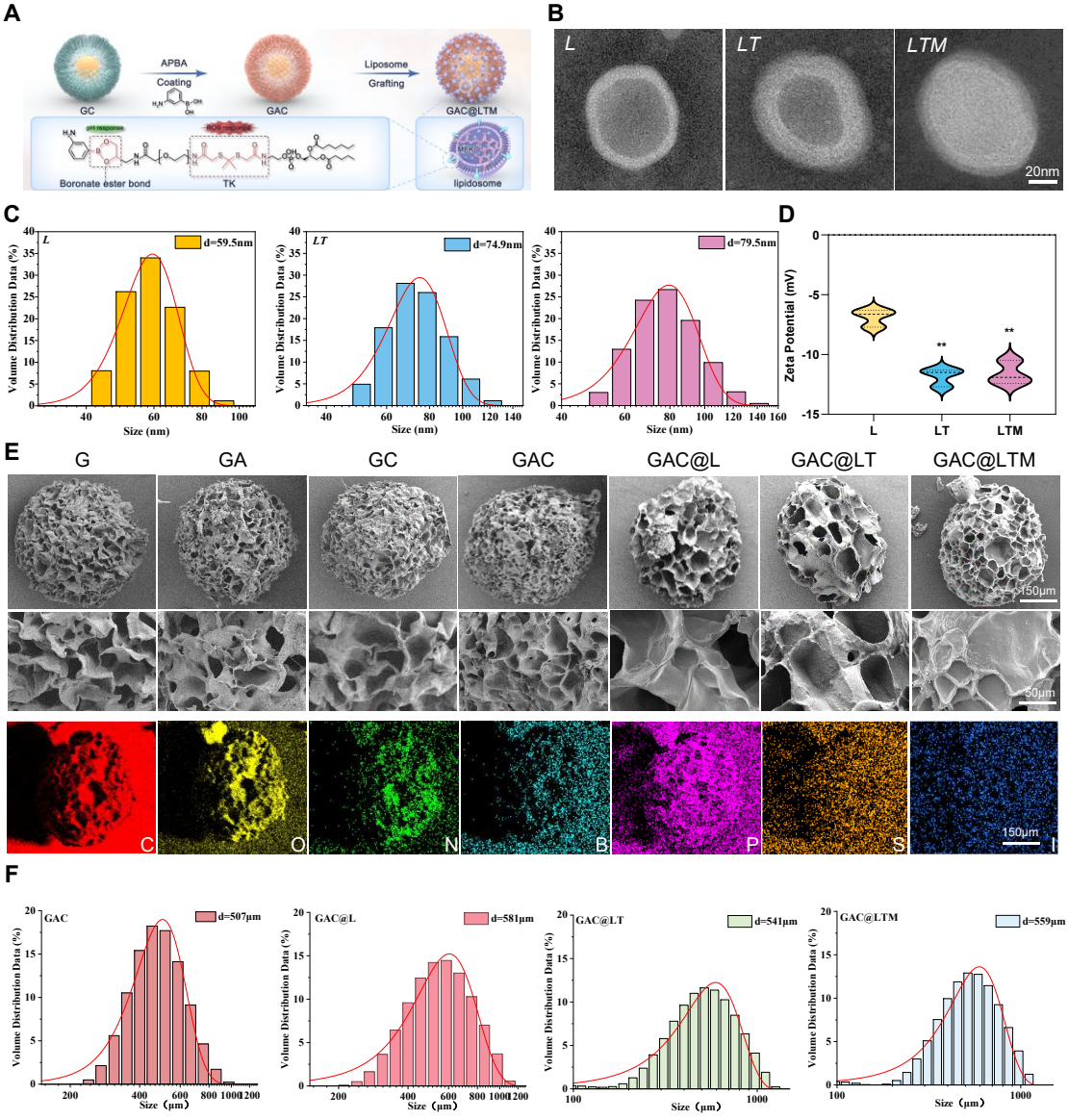


Fig. 3. Physical characterization of smart microsphere-liposome composite system. **A** Schematic diagram of the smart microsphere-liposome composite system. **B** Negative staining images of different liposomes. **C** Particle size analysis of different liposomes. **D** Zeta potential of different liposomes. **E** SEM images and EDS scans of the microsphere-liposome composite system. Scale bar = 150 μm. **F** Particle size analysis of the microsphere-liposome composite systems in each group. Mean ± SEM, $^{**}P < 0.01$.

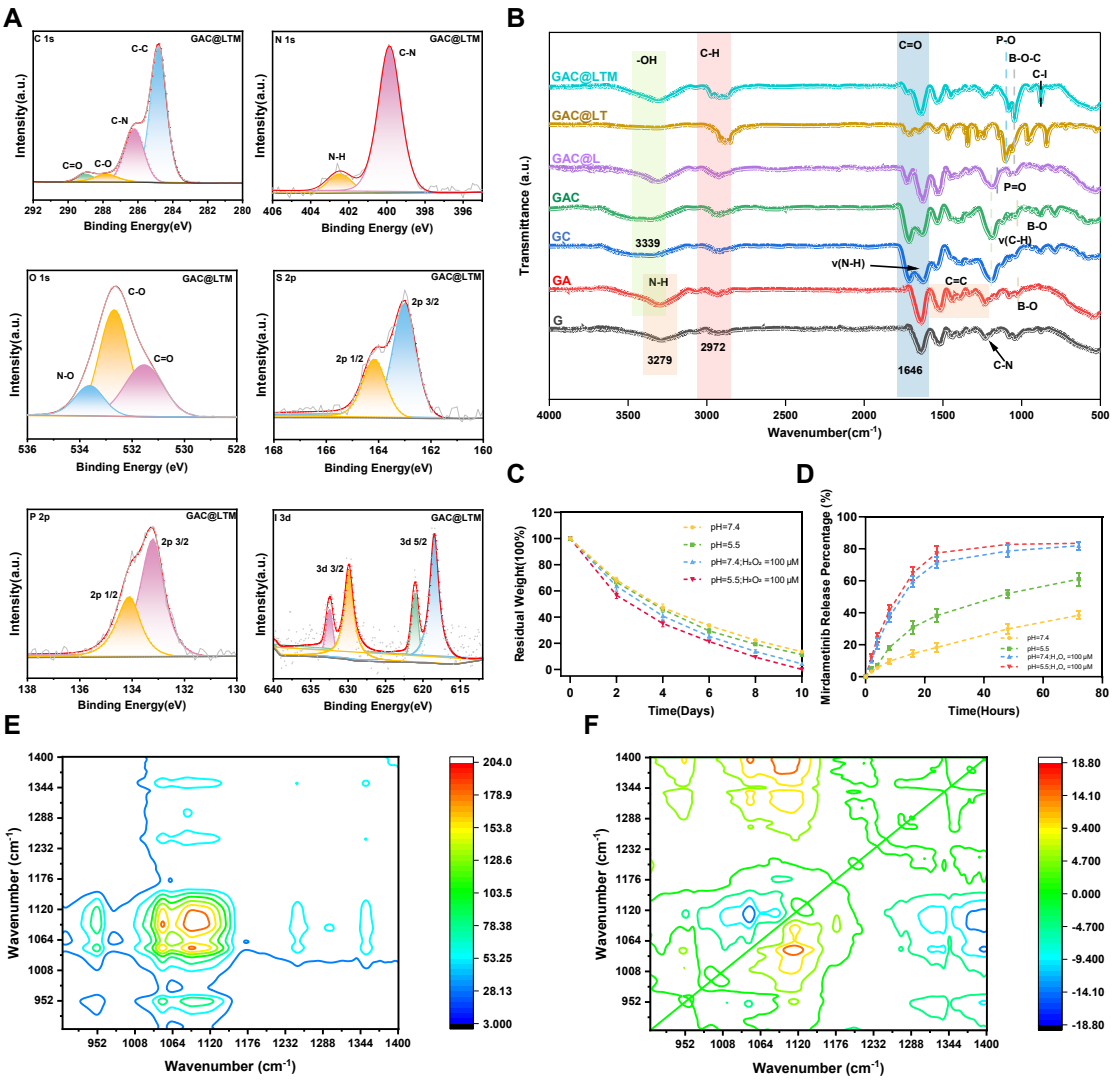


Fig. 4. Chemical characterization of smart microsphere-liposome composite system. **A** XPS detection spectrum of GAC@LTM. **B** Fourier transform infrared spectra for each group. **C** Degradation curves of GAC@LTM under different conditions. **D** Drug release curve of MEK inhibitor in GAC@LTM. **E** Synchronous plots of two-dimensional infrared detection for each group. **F** Asynchronous plots of two-dimensional infrared detection for each group.

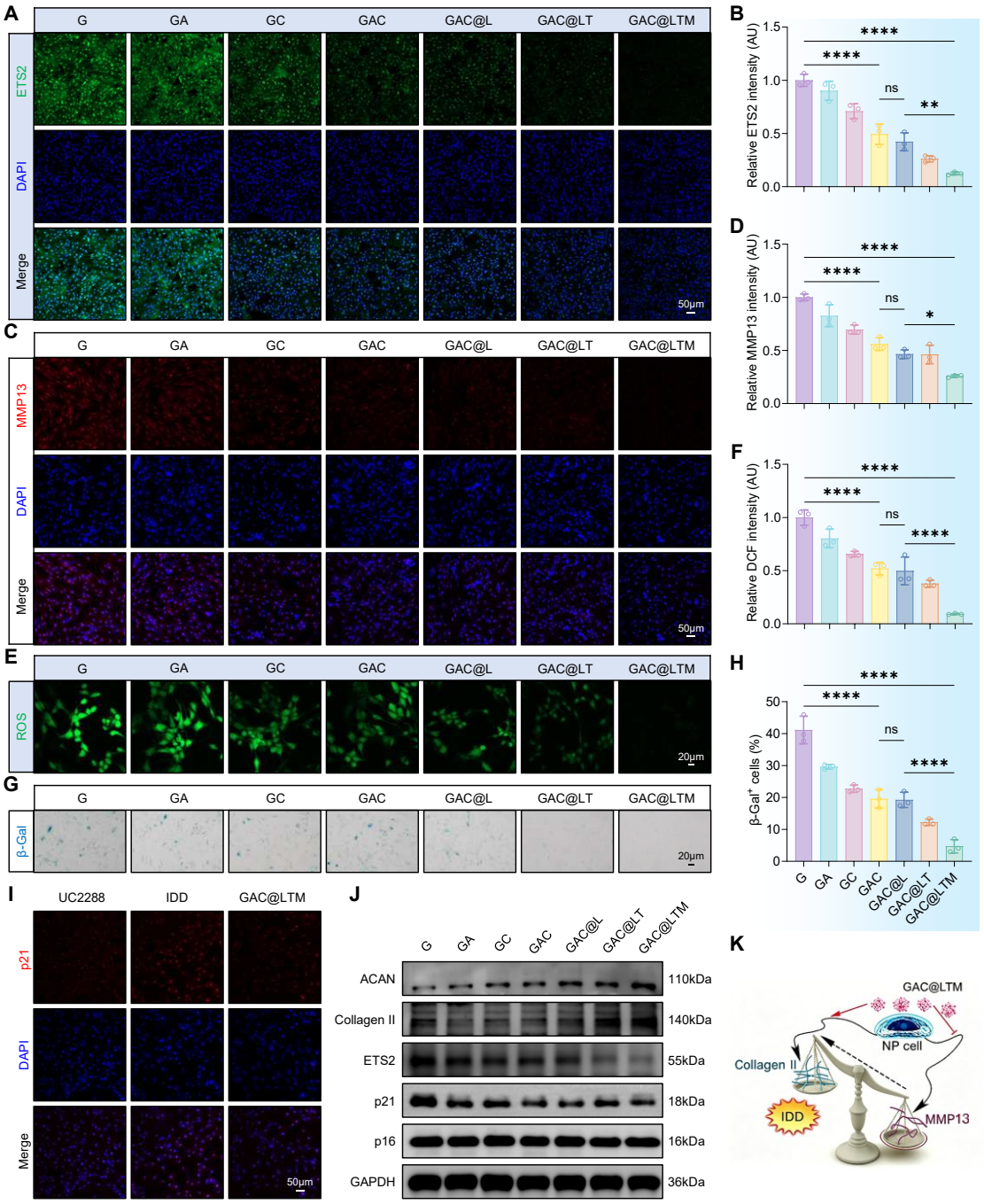


Fig. 5. Anti-inflammatory and anti-oxidant effects of GAC@LTM hydrogel. **A-D** Immunofluorescence and quantification of ETS2 and MMP13 expression in NPCs treated with TNF-α and hydrogel microspheres of different components for 24 h (n = 3). Scale bar = 50 μm. **E, F** Alleviation of oxidative stress in NPCs treated with TNF-α and hydrogel microspheres of different components for 24 h monitored by DCFH-DA (n = 3). Scale bar = 20 μm. **G, H** SA-β-gal staining and quantification of NPCs treated with TNF-α and hydrogel microspheres of different components for 24 h (n = 3). Scale bar = 20 μm. **I** Immunofluorescence of p21 expression in NPCs treated with TNF-α and GAC@LTM for 24 h. Scale bar = 50 μm. **J** Western blot of ACAN, Collagen II, ETS2,

p21 and p16 expression in NPCs treated with TNF-α and hydrogel microspheres of different components for 24 h. **K** Schematic diagram of GAC@LTM alleviating NPCs metabolic imbalance. Mean ± SEM, ns non-significant, *$P < 0.05$, **$P < 0.01$, ****$P < 0.0001$.

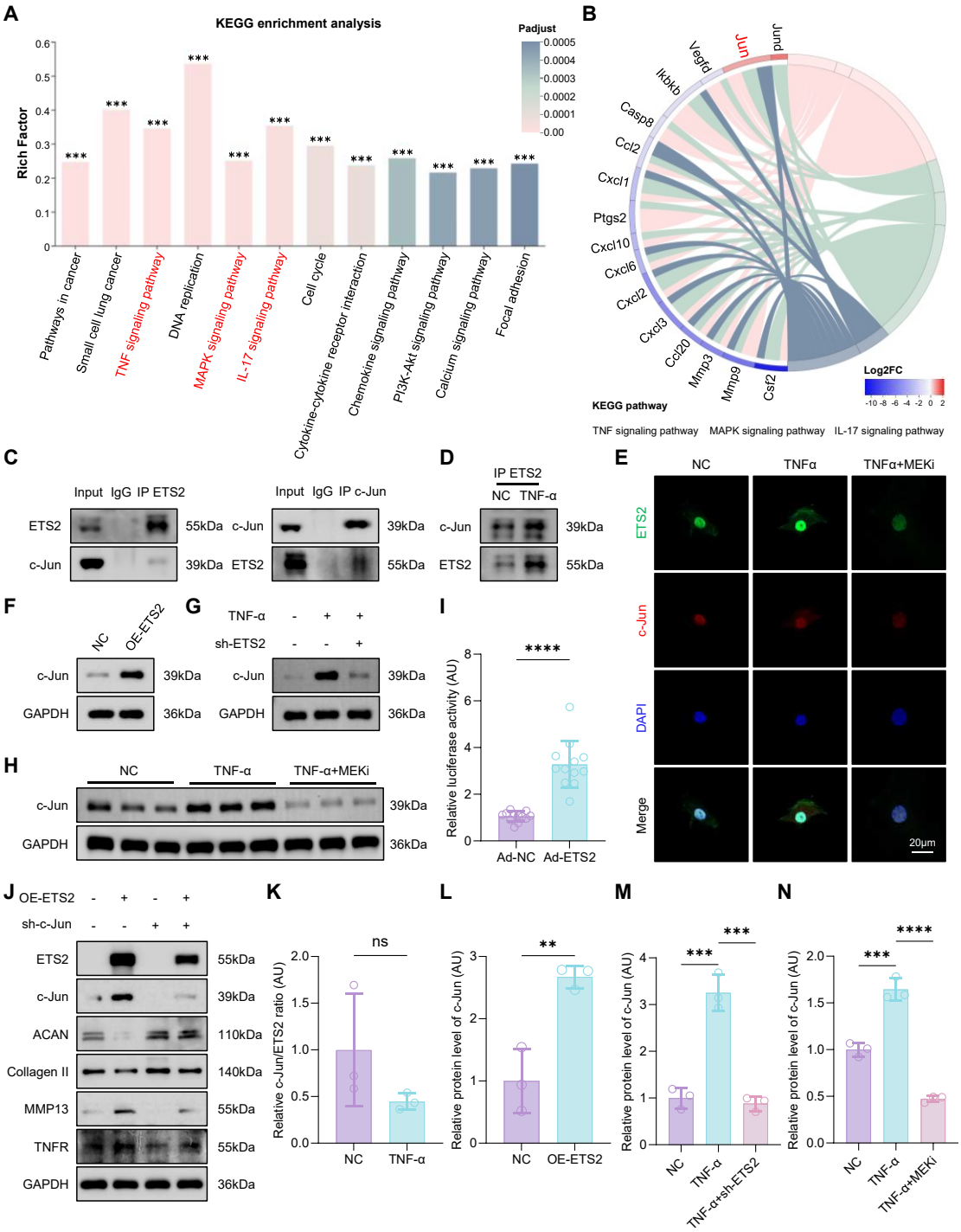


Fig. 6. ETS2 targets c-Jun to induce NPCs metabolic imbalance and inflammation. **A** KEGG enrichment histogram of RNA-seq. **B** Enriched chord diagram of RNA-seq. **C** Co-IP assay of NPCs to examine potential combination of ETS2 and c-Jun. **D**, **K** ETS2 was immunoprecipitated from NPCs after TNF-α treatment, and the presence of c-Jun in the immunoprecipitates was evaluated. **E** Immunofluorescence of ETS2 and c-Jun in NPCs treated with TNF-α and MEKi for 24 h. Scale bar = 20 μm. **F**, **L** Western blot and quantification of c-Jun expression in NPCs transfected with OE-ETS2 for 24 h (n = 3). **G**, **M** Western blot and quantification of c-Jun expression in NPCs transfected

with sh-ETS2 and treated with TNF-α for 24 h (n = 3). **H**, **N** Western blot and quantification of c-Jun expression in NPCs treated with TNF-α and MEKi for 24 h (n = 3). **I** Relative luciferase activity in HEK 293T cells transfected with OE-ETS2 for 24 h. **J** Western blot of c-Jun expression in NPCs transfected with OE-ETS2 and sh-c-Jun for 24 h. Mean ± SEM, ns non-significant, $^{**}P < 0.01$, $^{***}P < 0.001$, $^{****}P < 0.0001$.

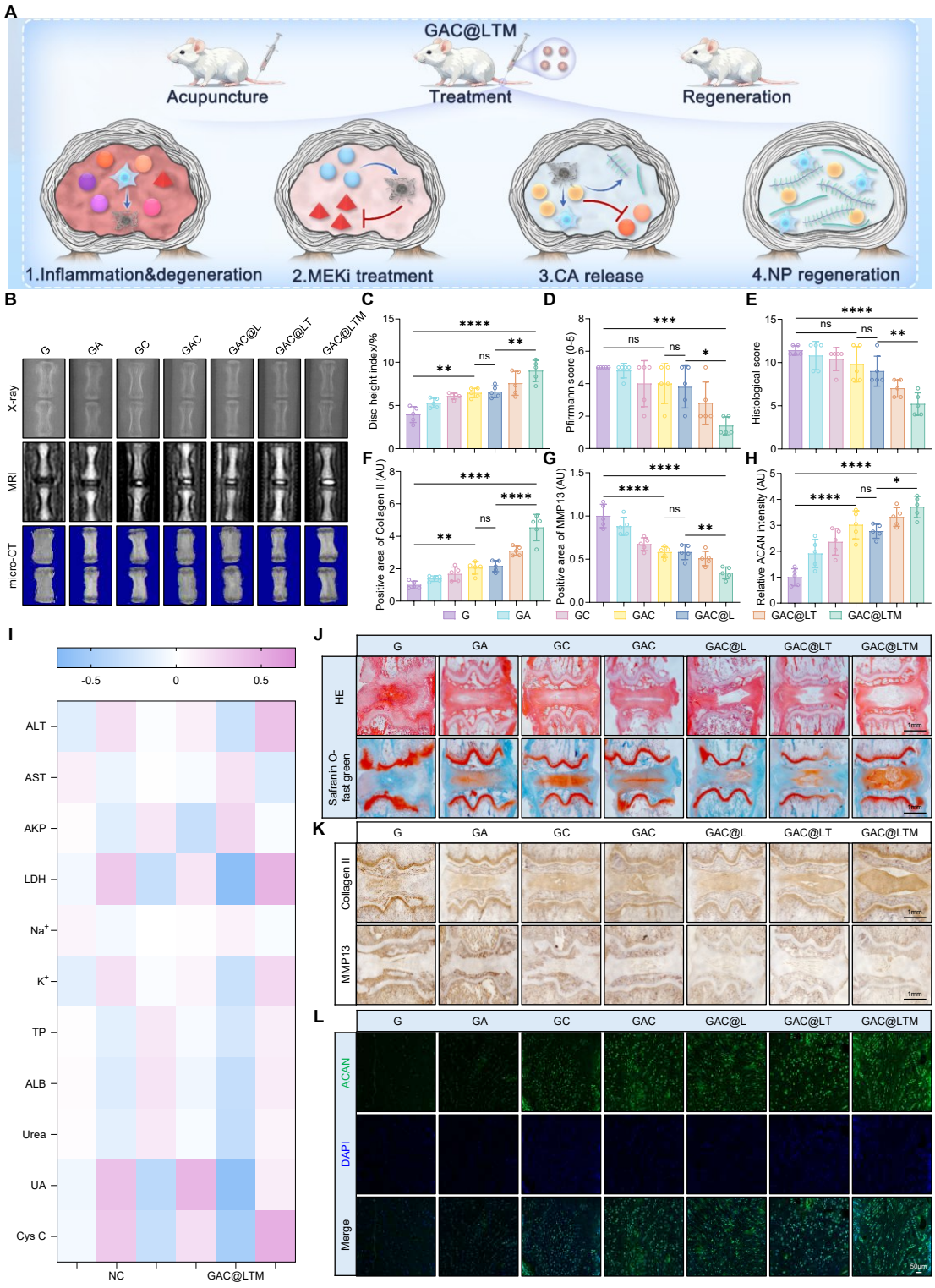
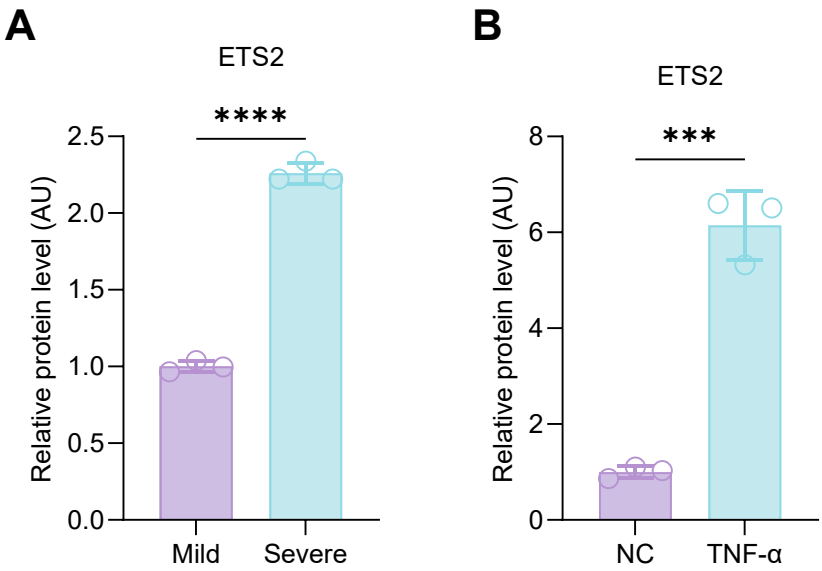
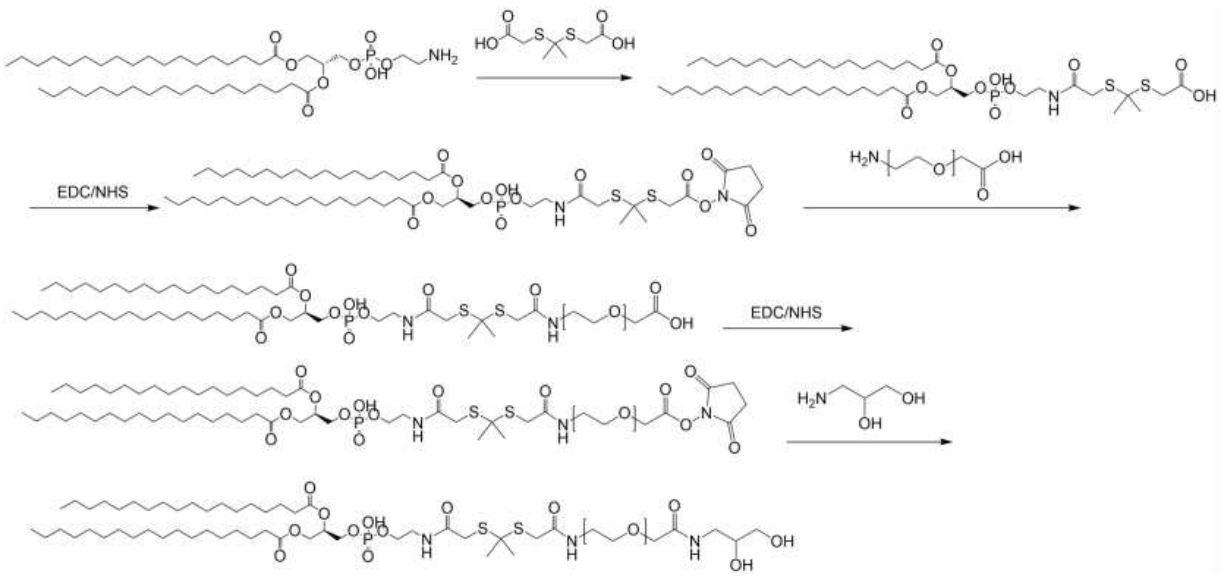


Fig. 7. GAC@LTM promotes NP tissue regeneration and alleviates IDD. **A** Schematic diagram of the process of rats receiving hydrogel microspheres of different components injections. **B** X-ray, MRI and micro-CT images of rat intervertebral discs. **C**, **D** Disc height index quantification and Pfirrmann score quantification. **E**, **J** Histological staining images and quantification of intervertebral discs at 4 weeks after treatment. Scale bar = 1000 μm. **F**, **G** and **K** Immunohistochemistry and

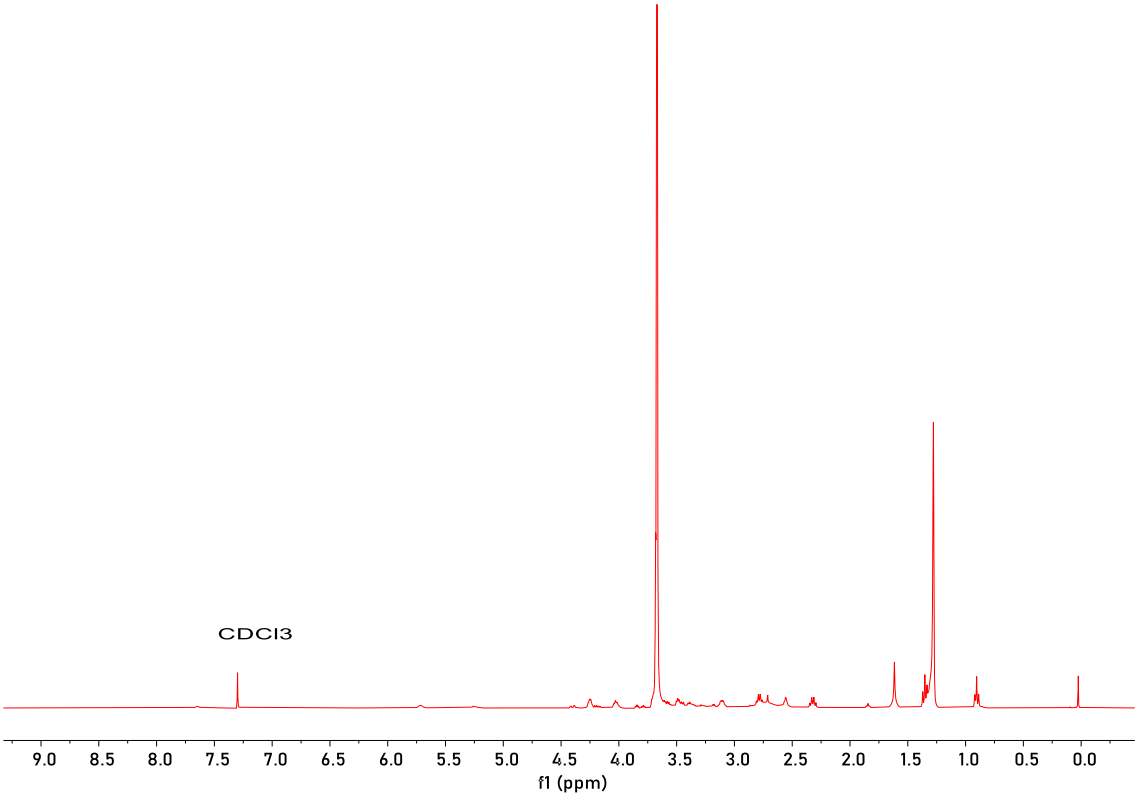
quantification of Collagen II and MMP13 expression of intervertebral discs at 4 weeks after treatment. Scale bar = 1000 μm. **H**, **L** Immunofluorescence and quantification of ACAN expression of intervertebral discs at 4 weeks after treatment. Scale bar = 50 μm. **I** Heatmap of blood biochemical tests. Mean ± SEM, ns non-significant, *$P < 0.05$, **$P < 0.01$, ***$P < 0.001$, ****$P < 0.0001$.



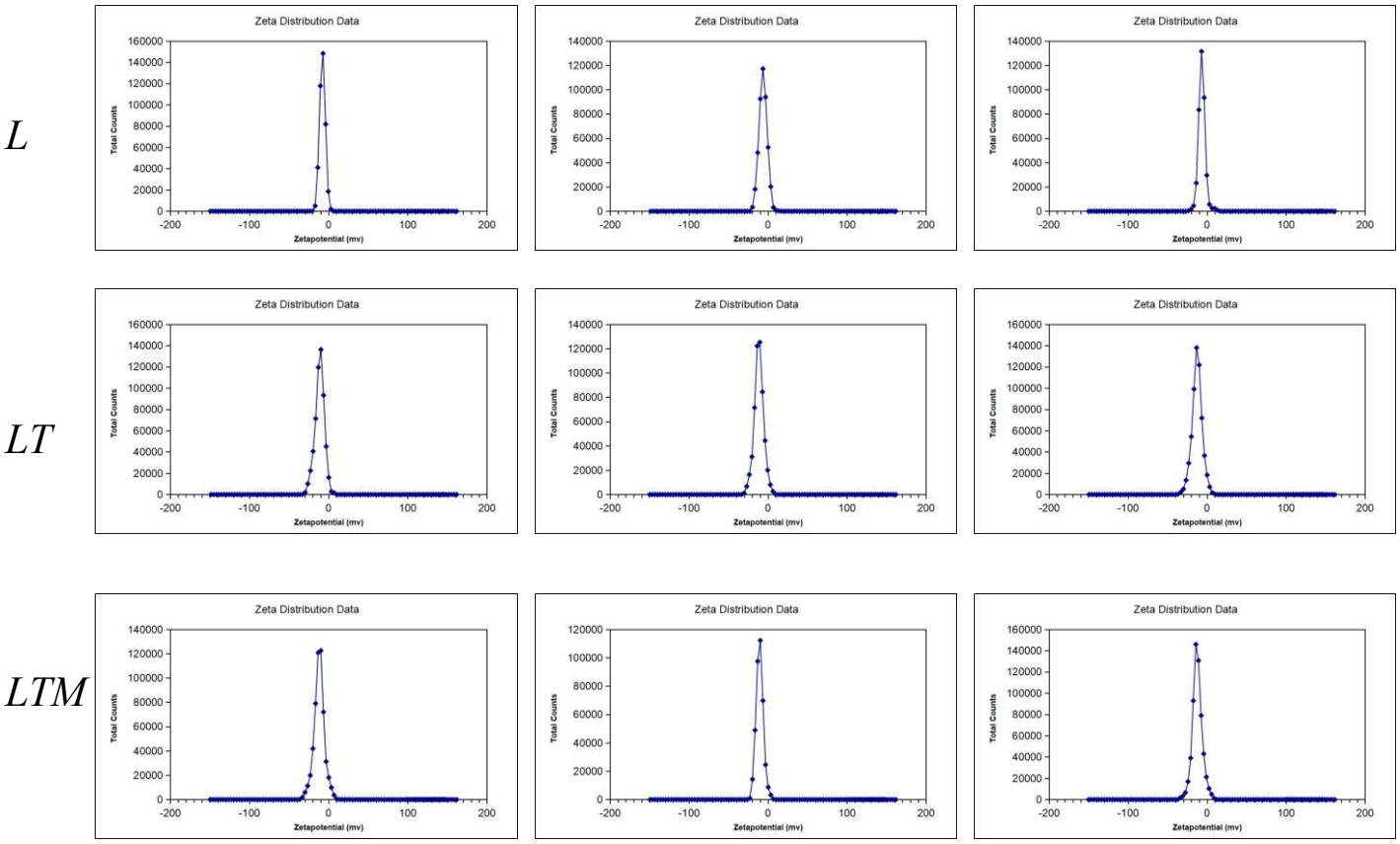
Supplementary Fig. 1. A Quantification of Western blot of ETS2 expression in clinical NP samples (n = 3). **B** Quantification of Western blot of ETS2 expression in NPCs treated with TNF-α for 24 h (n = 3).



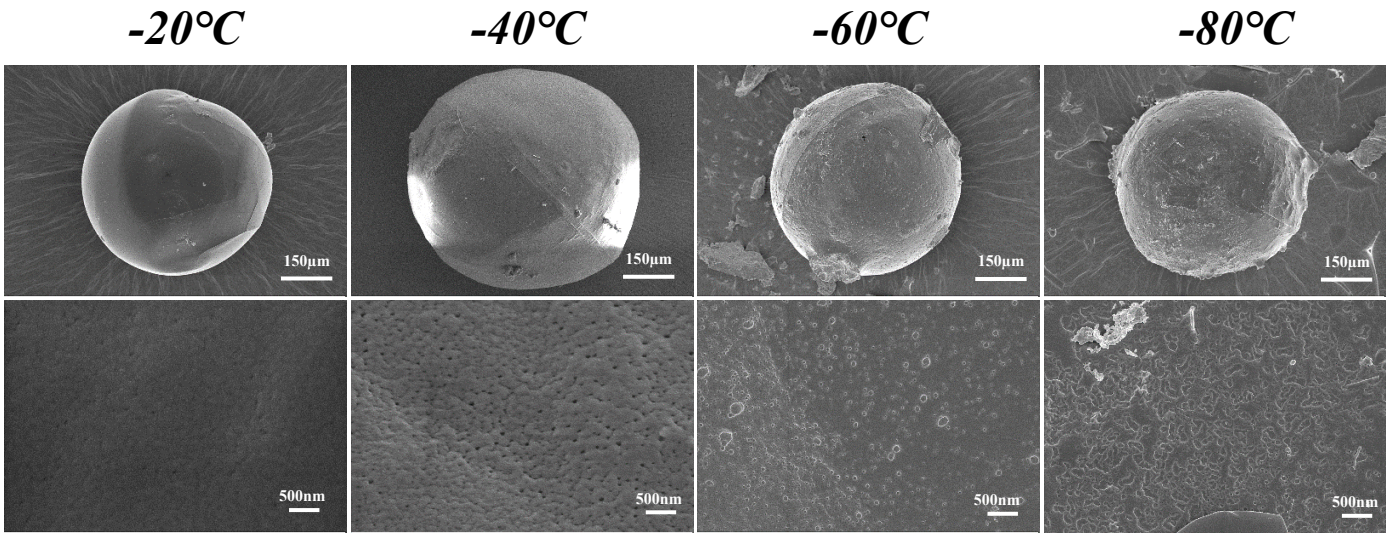
Supplementary Fig. 2. Roadmap for the synthesis of DSPE-TK-PEG2000 with an o-diol structure at the end



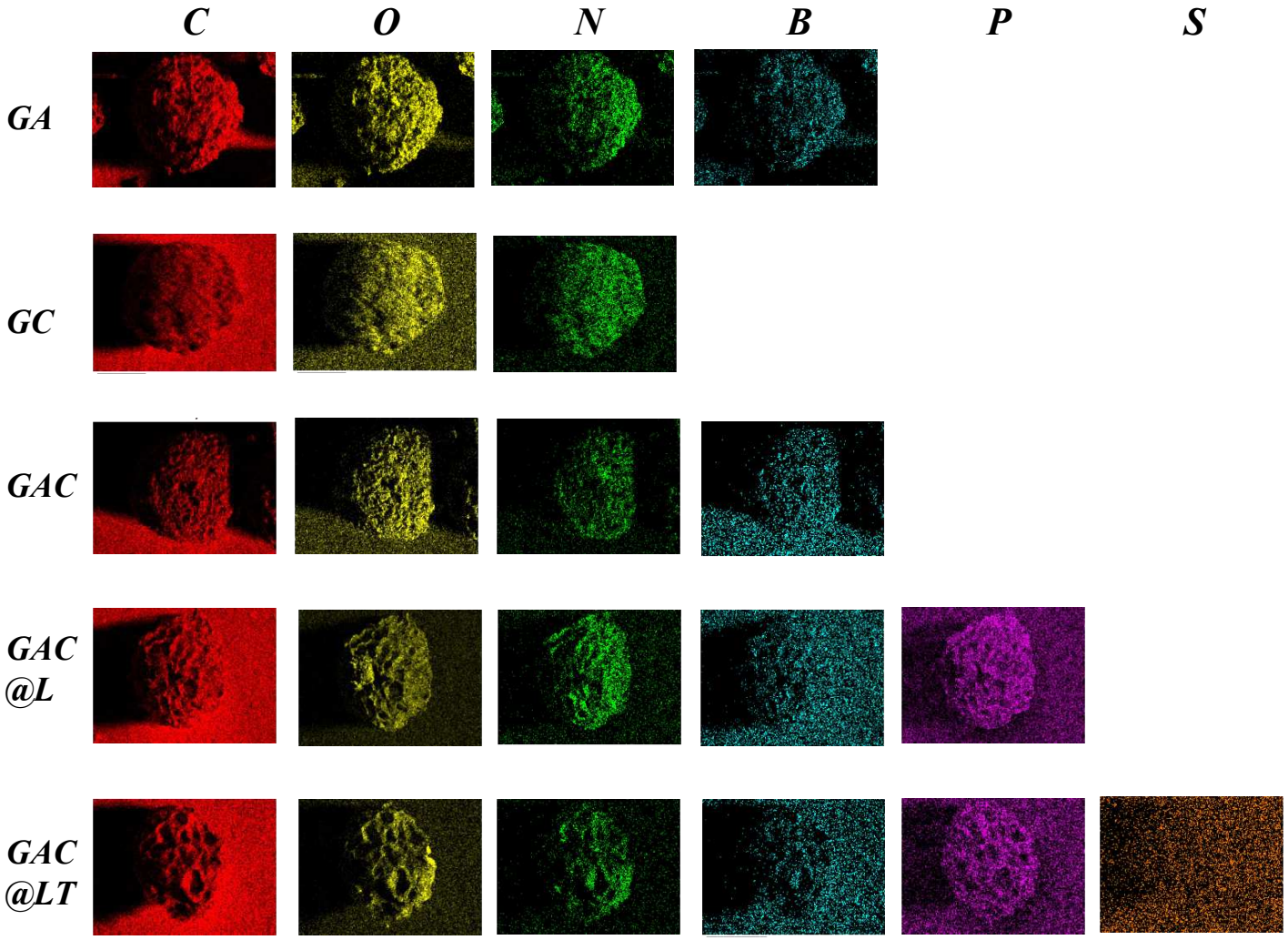
Supplementary Fig. 3. HPLC detection of DSPE-TK-PEG2000 with an o-diol structure at the end



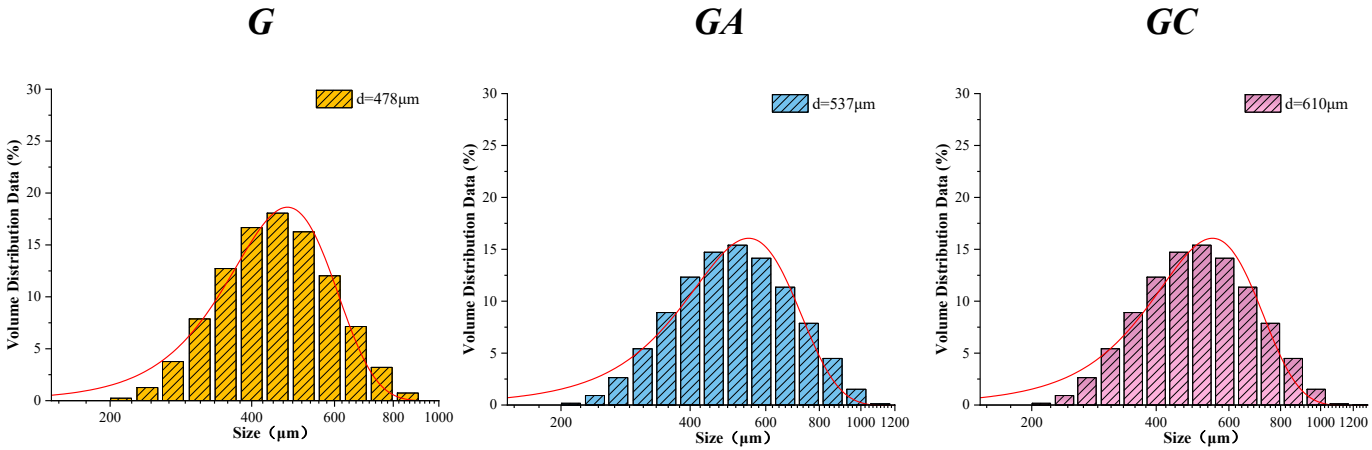
Supplementary Fig. 4. Plot of zeta potential of L, LT and LTM



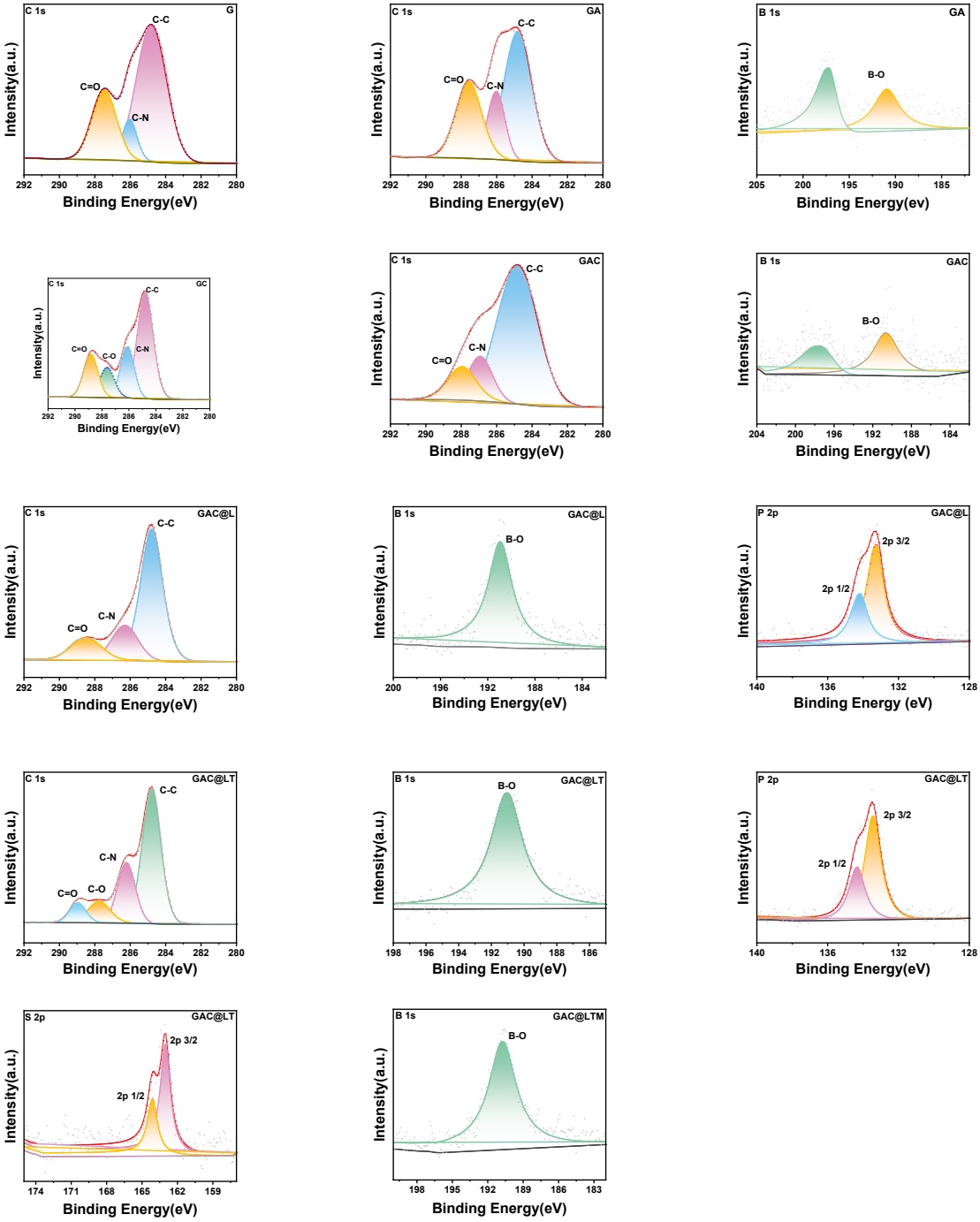
Supplementary Fig. 5. SEM images of GelMA under different processing conditions



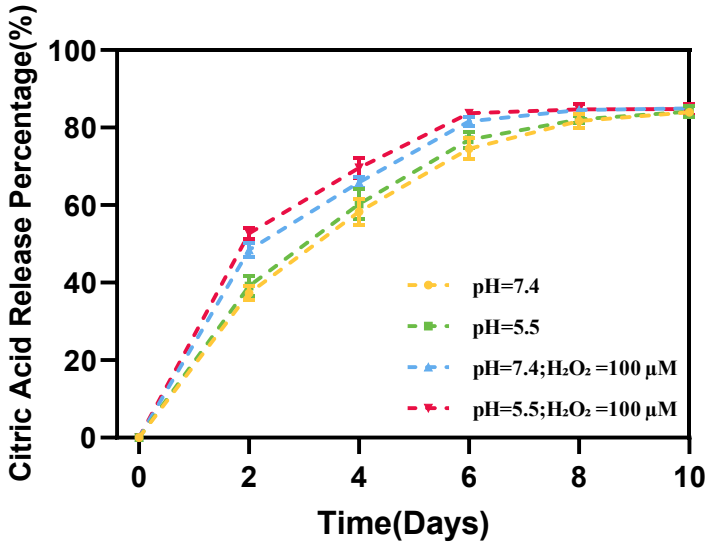
Supplementary Fig. 6. EDS scan images of each experimental group



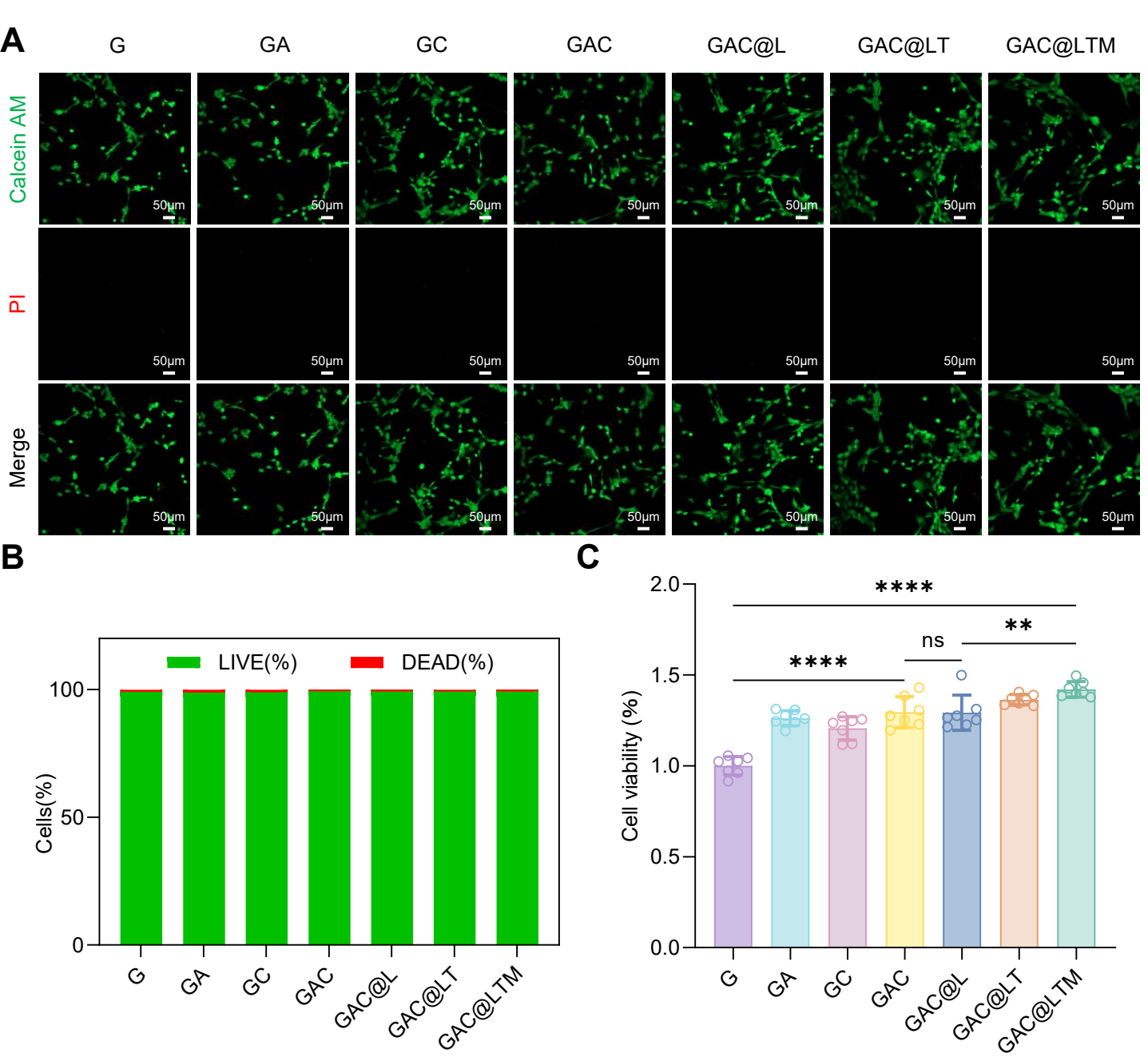
Supplementary Fig. 7. Particle size analysis



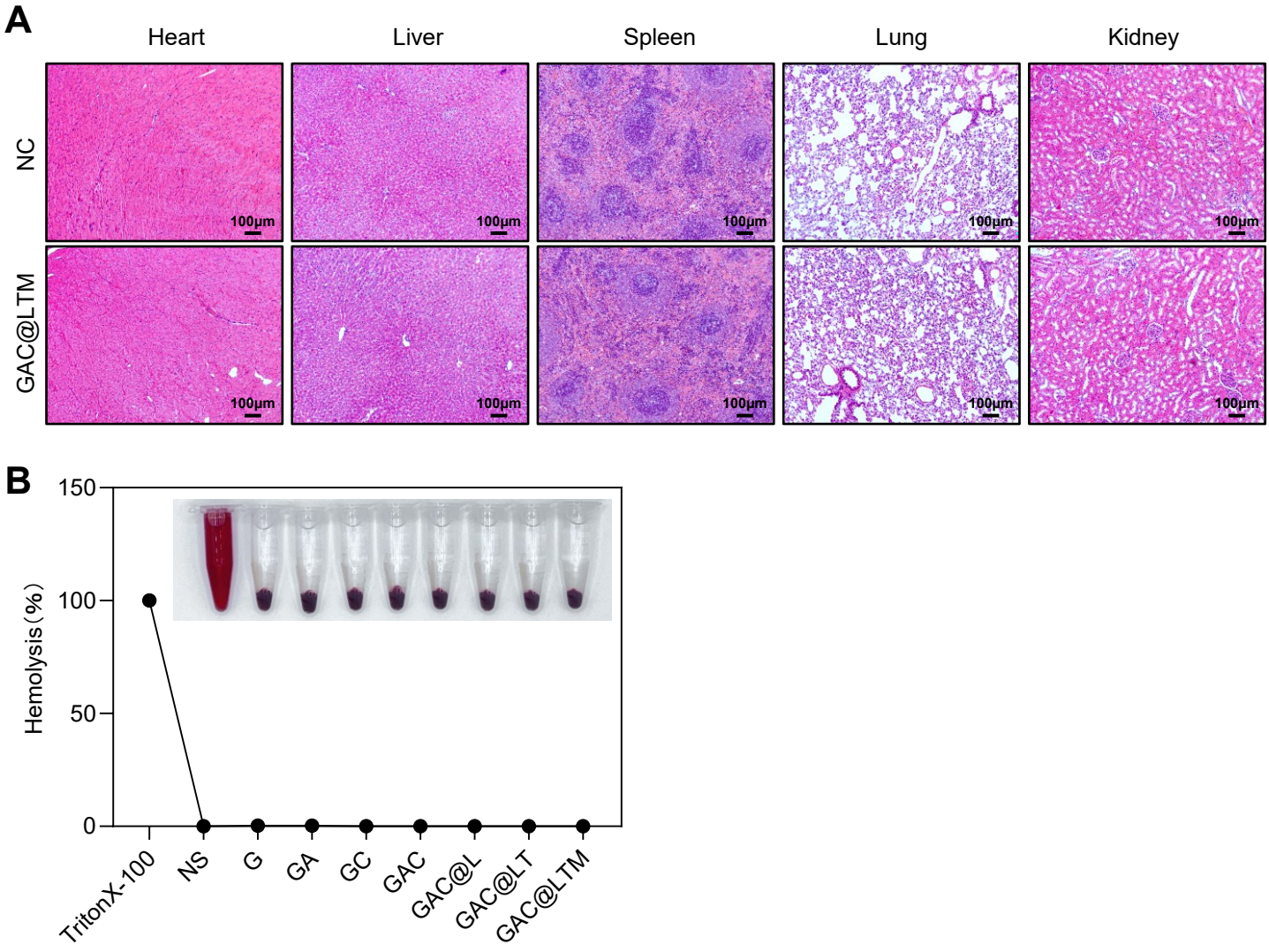
Supplementary Fig. 8. XPS assay for each group



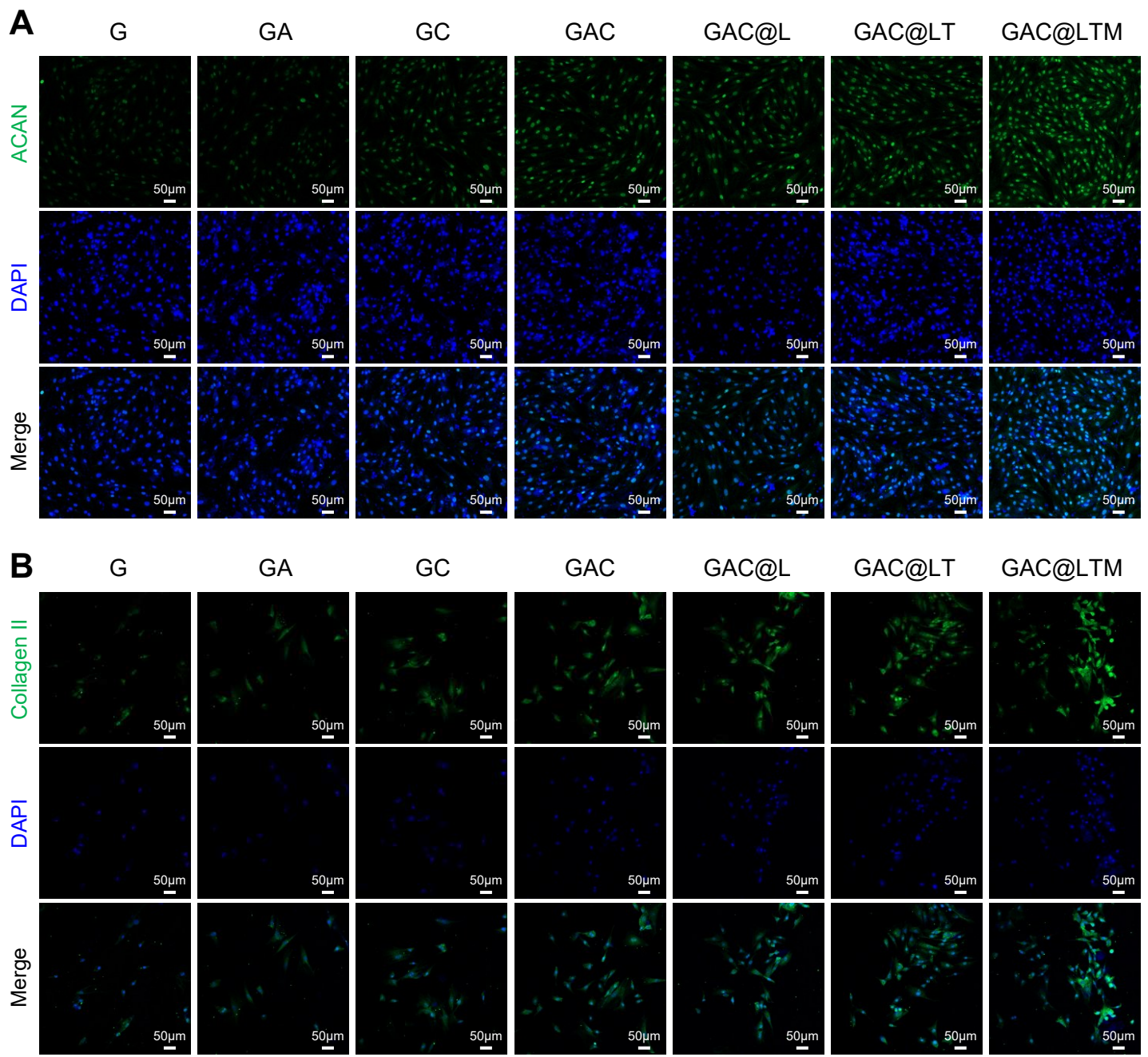
Supplementary Fig. 9. GAC@LTM citric acid drug release curve



Supplementary Fig. 10. A, B Live/dead cell staining and quantification of NPCs treated with hydrogel microspheres of different components for 24 h. **C** Cell viability of NPCs treated with hydrogel microspheres of different components for 24 h.



Supplementary Fig. 11. A HE staining of organs after treatment. **B** Hemolysis experiment after treatment.



Supplementary Fig. 12. A, B Immunofluorescence of ACAN and Collagen II expression of NPCs treated with TNF-α and hydrogel microspheres of different components for 24 h.

Supplementary Files

This is a list of supplementary files associated with this preprint. Click to download.

- SupplementalMaterial.pdf